

# Polarity mechanisms such as contact inhibition of locomotion regulate persistent rotational motion of mammalian cells on micropatterns

Brian A. Camley<sup>a,b</sup>, Yunsong Zhang<sup>c,d</sup>, Yanxiang Zhao<sup>b,e,f</sup>, Bo Li<sup>b,e</sup>, Eshel Ben-Jacob<sup>d,g</sup>, Herbert Levine<sup>d,h,1</sup>, and Wouter-Jan Rappel<sup>a,b</sup>

Departments of <sup>a</sup>Physics and <sup>b</sup>Mathematics and <sup>c</sup>Center for Theoretical Biological Physics, University of California, San Diego, La Jolla, CA 92093; Departments of <sup>d</sup>Physics and Astronomy and <sup>e</sup>Bioengineering and <sup>f</sup>Center for Theoretical Biological Physics, Rice University, Houston, TX 77005; <sup>g</sup>Department of Mathematics, The George Washington University, Washington, DC 20052; and <sup>h</sup>School of Physics and Astronomy, Tel Aviv University, Tel Aviv 6997801, Israel

Contributed by Herbert Levine, August 1, 2014 (sent for review June 30, 2014)

**Pairs of endothelial cells on adhesive micropatterns rotate persistently, but pairs of fibroblasts do not; coherent rotation is present in normal mammary acini and kidney cells but absent in cancerous cells. Why? To answer this question, we develop a computational model of pairs of mammalian cells on adhesive micropatterns using a phase field method and study the conditions under which persistent rotational motion (PRM) emerges. Our model couples the shape of the cell, the cell's internal chemical polarity, and interactions between cells such as volume exclusion and adhesion. We show that PRM can emerge from this minimal model and that the cell-cell interface may be influenced by the nucleus. We study the effect of various cell polarity mechanisms on rotational motion, including contact inhibition of locomotion, neighbor alignment, and velocity alignment, where cells align their polarity to their velocity. These polarity mechanisms strongly regulate PRM: Small differences in polarity mechanisms can create significant differences in collective rotation. We argue that the existence or absence of rotation under confinement may lead to insight into the cell's methods for coordinating collective cell motility.**

Collective cell migration is a crucial aspect of wound healing, growth and development of organs and tissues, and cancer invasion (1–3). Cells may move in cohesive groups ranging from small clusters of invading cancerous cells to ducts and branches during morphogenesis to monolayers of epithelial or endothelial cells. Two hallmarks of collective migration are strong cell–cell adhesion and multicellular polarity—an organization of the cellular orientation beyond the single-cell level (1). Cell–cell interactions can lead to collective behavior not evident in any single cell, including chemotaxis in clusters of cells that singly do not chemotax (4). Collective behavior may arise from cell–cell interactions altering the polarity of individual cells (5, 6). Many theories have been proposed for how this multicellular order appears, either in specific biological contexts (7–11) or in simpler, more generic models (12–16). Some authors argue that these dynamics are relatively universal and can be understood with minimal knowledge of the signaling pathways involved (2, 17).

Collective rotation is commonly observed in collectively migrating cells, especially in confinement. Persistent rotations have been observed in the slime mold *Dictyostelium discoideum* (18), canine kidney epithelial cells on adhesive micropatterns (19), and small numbers of endothelial cells on micropatterns (20, 21). Transient swirling patterns are also seen in epithelial monolayers (22). Recent work has also observed that the growth of spherical acini of human mammary epithelial cells in 3D matrix involves a coherent rotation persisting from a single cell to several cells; this rotation is not present in randomly motile cancerous cells (23). Similarly, cancerous cells on adhesive micropatterns do not develop coherent rotation (19). In a recent review of collective migration, Rørth (24) argues that “rotating movement seems to be a feature of normal epithelial cells when cultured under

spatially confined conditions”; however, the origin of collective rotation and its controlling factors remain unclear.

In this paper, we study a simple example of coordinated motion: the persistent rotational motion (PRM) of small numbers of mammalian cells crawling on micropatterned substrates. Huang et al. (20) and Huang and coworkers (21) observed that pairs of endothelial cells on islands of fibronectin robustly developed PRM in a “yin–yang” shape. By contrast, fibroblasts did not rotate, developing a straight, static interface between the two cells. We develop a computational model of multiple crawling mammalian cells that couples the cells' mechanical deformations to their biochemical polarity (asymmetry in a chemical species) and includes both mechanical and chemical cell–cell interactions. We use this model as a framework to understand which mechanical and chemical factors regulate robust PRM of cells on micropatterns. This simple system can lead to new insights into cell–cell interactions and multicell polarity and potentially exclude or refine certain mechanisms previously proposed as the cause of collective migration. We also suggest that the yin–yang cell–cell interface shape may reflect the influence of the nucleus, which is often not modeled.

## Model

We model physically interacting crawling cells with a chemical species  $\rho$  and a fluctuating inhibitor of  $\rho$ ,  $I$ .  $\rho$  orients the cell front;  $I$  controls cell persistence. We also model four “polarity mechanisms” that reorient cell polarity (e.g., by generating  $I$  at cell–cell contact). We extend the phase field description of a crawling eukaryotic cell as studied in Shao et al. (25) to study multiple cells interacting by volume exclusion and cell–cell

## Significance

**During the growth of an embryo or the spreading of a tumor, cells may travel collectively. We study a computational model of a simple example of collective migration: two cells confined to a square adhesive pattern. In this confinement, some cell types rotate, whereas others do not. We model these crawling cells, the forces between them, and several possible ways that the cells could choose what direction they will crawl—their “polarity mechanism.” We show that the cell polarity mechanism can control whether the pairs of cells rotate or remain fixed. This suggests that we can learn about how large groups of cells choose their direction by studying the rotation of pairs.**

Author contributions: B.A.C., B.L., E.B.-J., H.L., and W.-J.R. designed research; B.A.C., Y. Zhang, Y. Zhao, B.L., E.B.-J., H.L., and W.-J.R. performed research; and B.A.C., H.L., and W.-J.R. wrote the paper.

The authors declare no conflict of interest.

<sup>1</sup>To whom correspondence should be addressed. Email: herbert.levine@rice.edu.

This article contains supporting information online at [www.pnas.org/lookup/suppl/doi:10.1073/pnas.1414498111/-DCSupplemental](http://www.pnas.org/lookup/suppl/doi:10.1073/pnas.1414498111/-DCSupplemental).

adhesion. The phase field method has a long history of being used to study interfacial motion problems, including cell dynamics (26–31). Our model couples biochemical polarity, modeled by reaction–diffusion equations within the cell, and mechanical forces exerted by cells, including adhesive and repulsive forces between the two cells. For simplicity, we assume the interface motion is solely driven by local forces (25), neglecting fluid flow (32, 33). We treat cells as 2D, characterized by an interface with constant line tension  $\gamma$  and bending modulus  $\kappa$ . This interface is tracked by a “phase field”  $\phi(\mathbf{r})$  that smoothly varies from zero outside of the cell to unity inside it over a length scale  $\epsilon$ . We also model the nucleus of the cell with an additional phase field  $\nu(\mathbf{r})$ , treating it as an object with a fixed area as well as line tension  $\gamma_{\text{nuc}}$  and bending modulus  $\kappa_{\text{nuc}}$ . The nucleus moves freely subject to the constraint that it repels and is repelled by the cell membrane; this moves it to the back of the cell, consistent with ref. 20.

We describe two chemical components within the cell. First, the chemical polarity of the cell is determined by the concentration of a Rho GTPase  $\rho(\mathbf{r})$  that indicates the cell front (e.g., Rac or cdc42, an “actin promoter”). The Rho GTPase dynamics are given by a modification of the generic wave-pinning scheme of Mori et al. (34); this mechanism leads to a polarized cell with high  $\rho(\mathbf{r})$  defining the front and low  $\rho(\mathbf{r})$  characterizing the back of the cell. Second, we control the cell’s persistence of motion as well as potential cell–cell polarity coupling by introducing a fluctuating inhibitory field  $I(\mathbf{r})$  that deactivates  $\rho$ . Increasing the fluctuations of  $I$  decreases the persistence of the cell’s motion (SI Appendix, Fig. S2).

Each cell and nucleus has a phase field  $\phi^{(i)}(\mathbf{r})$ ,  $\nu^{(i)}(\mathbf{r})$ . From force balance, these obey (25) (see SI Appendix):

$$\partial_t \phi^{(i)}(\mathbf{r}, t) = \frac{1}{\tau} [\alpha \chi(\mathbf{r}) \rho^{(i)} - \beta] |\nabla \phi^{(i)}| - \frac{1}{\tau \epsilon} \frac{\delta H}{\delta \phi^{(i)}} \quad [1]$$

$$\partial_t \nu^{(i)}(\mathbf{r}, t) = -\frac{M}{\tau_{\text{nuc}}} (A_\nu^{(i)} - A_{\text{nuc}}) |\nabla \nu^{(i)}| - \frac{1}{\tau_{\text{nuc}} \epsilon} \frac{\delta H}{\delta \nu^{(i)}}. \quad [2]$$

The first term on the right of Eq. 1 is the active motion of the membrane driven by actomyosin forces: The cell membrane is pushed radially outward at the cell front, where  $\alpha \chi \rho > \beta$ , but contracts at the back, where  $\alpha \chi \rho < \beta$ .  $\alpha$  sets the protrusion strength,  $\beta$  sets the contraction strength, and  $\tau$  is a friction coefficient. We hypothesize, following the logic of ref. 33, that protrusion does not occur when the cell cannot adhere to the micropattern, and therefore define  $\chi(\mathbf{r})$  to be unity on the micropattern and zero off it. The second term of Eq. 1 shows that the phase field will, in the absence of actomyosin driving forces, minimize a Hamiltonian  $H$ . This energy, which will be discussed below, includes contributions from the deformation of the membrane, membrane–nucleus exclusion, and cell–cell interactions. We are modeling cells that may spread, and thus do not fix their area (see, e.g., ref. 35).

The dynamics of the cell nucleus in Eq. 2 similarly minimizes  $H$  but has no active driving force. Instead, we model the nucleus as effectively incompressible and implement a penalty term that contracts (expands) the nucleus isotropically when its area  $A_\nu = \int d^2r \nu(\mathbf{r})$  is larger (smaller) than the prescribed area  $A_{\text{nuc}}$ .  $M$  is the strength of this penalty term and  $\tau_{\text{nuc}}$  the friction coefficient for nuclear motion.

The Hamiltonian is given by

$$H = \sum_{i=1}^{n_c} H_{\text{single cell}}[\phi^{(i)}, \nu^{(i)}] + H_{\text{cell–cell}}, \quad [3]$$

where  $H_{\text{single cell}}[\phi, \nu] = H_\phi[\phi] + H_\nu[\nu] + H_{\text{nuclear constraint}}[\phi, \nu]$  and  $n_c$  is the number of cells. The phase-field energy for  $\phi$  is

$$H_\phi = \gamma \int d^2r \left[ \frac{\epsilon}{2} |\nabla \phi|^2 + \frac{G(\phi)}{\epsilon} \right] + \frac{\kappa}{2} \int d^2r \frac{1}{\epsilon} \left[ \epsilon \nabla^2 \phi - \frac{G'(\phi)}{\epsilon} \right]^2,$$

where  $G(\phi) = 18\phi^2(1 - \phi)^2$  is a double-well potential that is minimized by  $\phi = 0$  (cell exterior) and  $\phi = 1$  (cell interior). Here,  $\gamma$  is the interface tension and  $\kappa$  its bending modulus. In the sharp-interface limit  $\epsilon \rightarrow 0$ ,  $H_\phi$  becomes the usual Canham–Helfrich Hamiltonian (36, 37) for a fluid membrane (see refs. 38 and 39).  $H_\nu$  is given by an identical form with  $\phi$  replaced by  $\nu$  and different parameters  $\gamma_{\text{nuc}}$  and  $\kappa_{\text{nuc}}$ . We model the cell–nucleus interaction by imposing a simple energy penalty if the nucleus begins to exit the cell,  $H_{\text{nuclear constraint}} = g_{\text{nuc}} \int d^2r [1 - \phi(\mathbf{r})] \nu(\mathbf{r})$ . We model two physical cell–cell interactions, a repulsion between cell bodies and an attraction between cell interfaces, using a variant of the method of Nonomura (40). Excluded volume is modeled by penalizing cell overlap, and the adhesion interaction promotes membrane–membrane contact between cells.

$$H_{\text{cell–cell}} = \sum_{i \neq j} \int d^2r \left[ \frac{g}{2} \phi^{(i)}(\mathbf{r}) \phi^{(j)}(\mathbf{r}) - \frac{\sigma \epsilon^3}{4} |\nabla \phi^{(i)}|^2 |\nabla \phi^{(j)}|^2 \right]$$

$g$  penalizes overlap area between the two cells.  $\sigma$  controls the energy of adhesion but is not precisely the energy of adhesion per length of overlap (SI Appendix).

We model chemical concentrations within the cell with reaction–diffusion equations. To solve these equations in the moving and deforming cell interior, we use the phase field method (25, 26, 30), which has numerically and analytically been shown to reproduce reaction–diffusion dynamics with no-flux boundary conditions (26, 30). Our equations for the Rho GTPase  $\rho$  and the fluctuating inhibitor  $I$  in each cell are

$$\partial_t (\phi^{(i)} \rho^{(i)}) = \nabla \cdot [\phi^{(i)} D_\rho \nabla \rho^{(i)}] + f_{f_\rho}(\rho^{(i)}, \rho_{\text{cvt}}^{(i)}, I^{(i)}), \quad [4]$$

$$\partial_t (\phi^{(i)} I^{(i)}) = \nabla \cdot [\phi^{(i)} D_I \nabla I^{(i)}] + f_{f_I}(I^{(i)}, \{\phi\}, \{I\}), \quad [5]$$

where  $D_{\rho, I}$  are diffusion coefficients and  $f_{\rho, I}$  are reaction terms.  $f_\rho$  describes an exchange between active, membrane-bound Rho GTPase,  $\rho(\mathbf{r})$  and a uniform cytosolic pool  $\rho_{\text{cvt}}$ ;  $\rho(\mathbf{r})$  actively recruits cytosolic Rho GTPase, and positive (negative)  $I$  increases (decreases) the transition rate of  $\rho \rightarrow \rho_{\text{cvt}}$ . This model, a variant of the generic scheme proposed by Mori et al. (34), can create a steady-state distribution of  $\rho$  such that one side of the cell (the front) has high  $\rho$  and the other side has low  $\rho$ .  $f_I$  includes a spatially

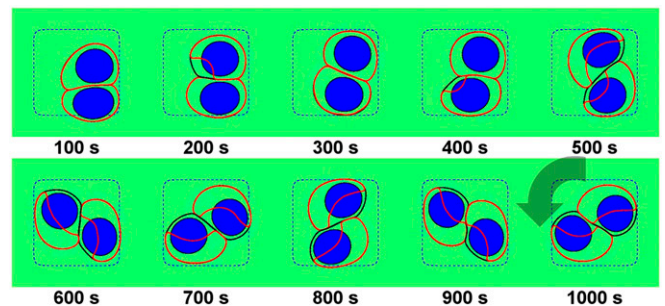


**Fig. 1.** Persistent rotational motion can be recreated in our minimal model. Parameters are listed in SI Appendix;  $L_{\text{micro}} = 30 \mu\text{m}$ . In this figure, and throughout the paper, the cell membrane is indicated by a black line, the Rho GTPase  $\rho$  by a red contour showing the points where  $\rho = \max(\rho\phi)/2$ , the cell nucleus by a blue shape, and the micropattern by a blue dashed line (SI Appendix, Fig. S1 provides a legend). See also Movie S1.

and temporally uncorrelated noise as well as a decay of  $I$  over time. We will also use the term  $f_I$  to model couplings between cell–cell contact and polarity. For instance, we will model “contact inhibition of locomotion” in which cell–cell contact locally generates  $I$ . The full reaction terms are shown in *SI Appendix*.

## Results

**Pairs of Confined Cells Can Develop Persistent Rotation but Also May Stall.** In our simulations of pairs of cells on a square micropattern we can observe PRM in a minimal model without explicit cell–cell alignment interactions (Fig. 1). To observe rotation, we have chosen the parameters of the model such that the cells are highly persistent and are strongly adherent. We also set parameters such that cell spread area is smaller than the micropattern, so free- and confined-cell morphologies are similar. Parameters are listed in *SI Appendix, Table S1*.

In Fig. 1, we show a simulation where our cells develop PRM, but other results occur, even with identical parameters. In Fig. 2, we show representative snapshots of simulations with different initial conditions. We find rotational motion in only 5/30 cases (see *SI Appendix* for distribution of initial conditions). Non-rotating cell pairs have two common morphologies: cells stuck in either opposing corners of the micropattern or a single corner; we also see transient cases with one or more cell unpolarized and one case of rotation stopping (*Movie S1*). PRM is completely inhibited on smaller micropatterns ( $L_{\text{micro}} = 25 \mu\text{m}$ ); in this case, the cell spread area is constricted, preventing polarization (33, 34, 42).

### Rotational Motion Is Strongly Regulated by Cell Polarity Mechanisms.

In our studies of PRM above, we assumed that the presence of the other cells does not directly influence the underlying chemical polarity of any cell, except via mechanical interactions. This minimal model creates a persistent cohort rotation (although not robustly). However, the existence of direct interactions between the polarity of neighboring cells has been well established, including contact inhibition of locomotion in neural crest cells and fibroblasts (3–5, 43, 44) and polarity induced by stress on cadherin adhesions of mesendoderm cells (6). We argue that effects of this type must be included in realistic models of PRM. Many polarity-regulating mechanisms have also been shown to create collective cell migration in simulations. These include extensions of flocking models of birds in which cell polarity (and hence velocity) become aligned with cell neighbor velocities (11, 14, 18, 45), models where polarity becomes aligned with the cell’s velocity or displacement (13, 15, 17, 46–48), and more directly experimentally inspired mechanisms including contact inhibition of locomotion (10, 12). We are interested in studying the role of these polarity-control mechanisms in establishing persistent rotation and cohort migration in these small systems, which may provide a useful testing ground for effects beyond the more universal features of alignment in larger systems.

We implement within our cell model four generic types of polarity-alignment mechanisms (Fig. 3): (i) neighbor alignment

(NA), in which cells align their polarity to the average velocity of the cells in the neighborhood (e.g. 14, 18, 45); (ii) velocity alignment (VA), in which cells align their polarity to their own velocity (13, 15, 47, 48); (iii) contact inhibition of locomotion (CIL), in which cell polarity is inhibited by contact with other cells (10, 12); and (iv) cell front–front inhibition (FF), a generalization of CIL in which only contact with the cell front is inhibitory. FF is supported by experiments of Desai et al. (49) that show head–head collisions lead to repolarization at a greater rate than head–tail collisions. There is also some historical precedent; in early papers on CIL, Abercrombie and Dunn (44) argued for a distinction between head–head and head–tail collisions; see also ref. 43 for a discussion of this point. For details of the implementation of these polarity types, see *SI Appendix*.

In Fig. 3 we present simulations of pairs of cells with these four different polarity mechanisms. We discover that of these four generic models VA robustly promotes the presence of PRM, CIL completely eliminates rotation, and NA promotes the linear motion of cells in an aligned flock but inhibits PRM. FF promotes PRM, but only if the cells are sufficiently confined ( $L_{\text{micro}} = 25 \mu\text{m}$ ); in micropatterns with  $L_{\text{micro}} = 30 \mu\text{m}$ , the FF mechanism leads to static cells. These general trends persist even if our parameters are varied, unless cell motility is inhibited by the parameter changes (*SI Appendix, Tables S2–S5 and Fig. S7*); complete loss of cell–cell adhesion also disrupts PRM in FF (*SI Appendix, Fig. S7C*).

CIL generates the inhibitor  $I(\mathbf{r})$  at cell–cell contact. In Fig. 3, we see that the  $I(\mathbf{r})$  at the cell interface ensures that the cells polarize directly away from one another, preventing any rotation. As the cells remain in contact,  $I(\mathbf{r})$  is still generated at the interface, ensuring that the cells maintain their polarity pointing away from the contact.

FF cells initially resemble CIL cells, but when the front of one cell touches the back of another the chiral symmetry of the pair is broken, leading to rotation. However, in the  $L_{\text{micro}} = 30 \mu\text{m}$  micropattern, FF cells cannot effectively make and maintain this symmetry-breaking contact, and the FF mechanism actually suppresses PRM (*SI Appendix, Fig. S3*).

NA cells are successful at creating a sort of collective motion—they do remain aligned with each other. However, the strong alignment between cells prevents the development of PRM. Instead, pairs of NA cells travel as a “flock,” moving from one side of the pattern to the other, then reversing. This is relatively unsurprising, because the NA mechanism is commonly used to describe flocking of birds (14). Similar mechanisms can, however, create collective rotation in a larger collection of cells, where local alignment is compatible with rotation (18).

When the VA mechanism is imposed, cells impact the boundary and then reorient, because their velocity is no longer outwardly directed; this reorientation ensures that cells do not become trapped at the boundary, as occurs in the default mechanism. PRM occurs in VA cells in both 25- $\mu\text{m}$  and 30- $\mu\text{m}$  micropatterns. However, “flocking” motions are also seen (transiently in 25- $\mu\text{m}$  patterns and occasionally in 30- $\mu\text{m}$  patterns; *Movies S6 and S10*); flocking can be suppressed by increasing the noise strength  $\zeta$  (*Movie S11*).

**Rotational Motion Is Disrupted in Cells with Lower Persistence.** We have shown that the presence and robustness of PRM can be controlled by polarity-alignment mechanisms. However, persistent rotational motion also requires that the cell’s linear motion be sufficiently persistent; as the model of Huang et al. (20) makes clear, cells that undergo effectively pure random-walk motility are not likely to develop rotation. In our model, the persistence time (as measured from the cell’s velocity–velocity correlation function) is controlled by the amplitude of the fluctuating source term in the  $I(\mathbf{r})$  equation. We show in *SI Appendix, Fig. S4 and Movie S12* that decreasing cell persistence also disrupts persistent motion in our model, as expected.

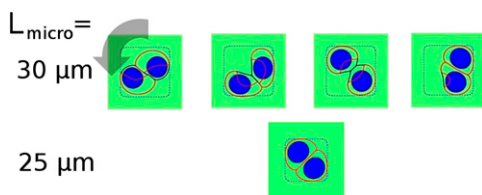


**Fig. 2.** PRM with the minimal model is not robust, and does not exist on small micropatterns. We show typical states of our simulation of two confined cells at 1,000 s. (Upper) Micropattern size  $L_{\text{micro}} = 30 \mu\text{m}$ . (Lower) Micropattern size  $L_{\text{micro}} = 25 \mu\text{m}$ . See also *Movies S1 and S2*.

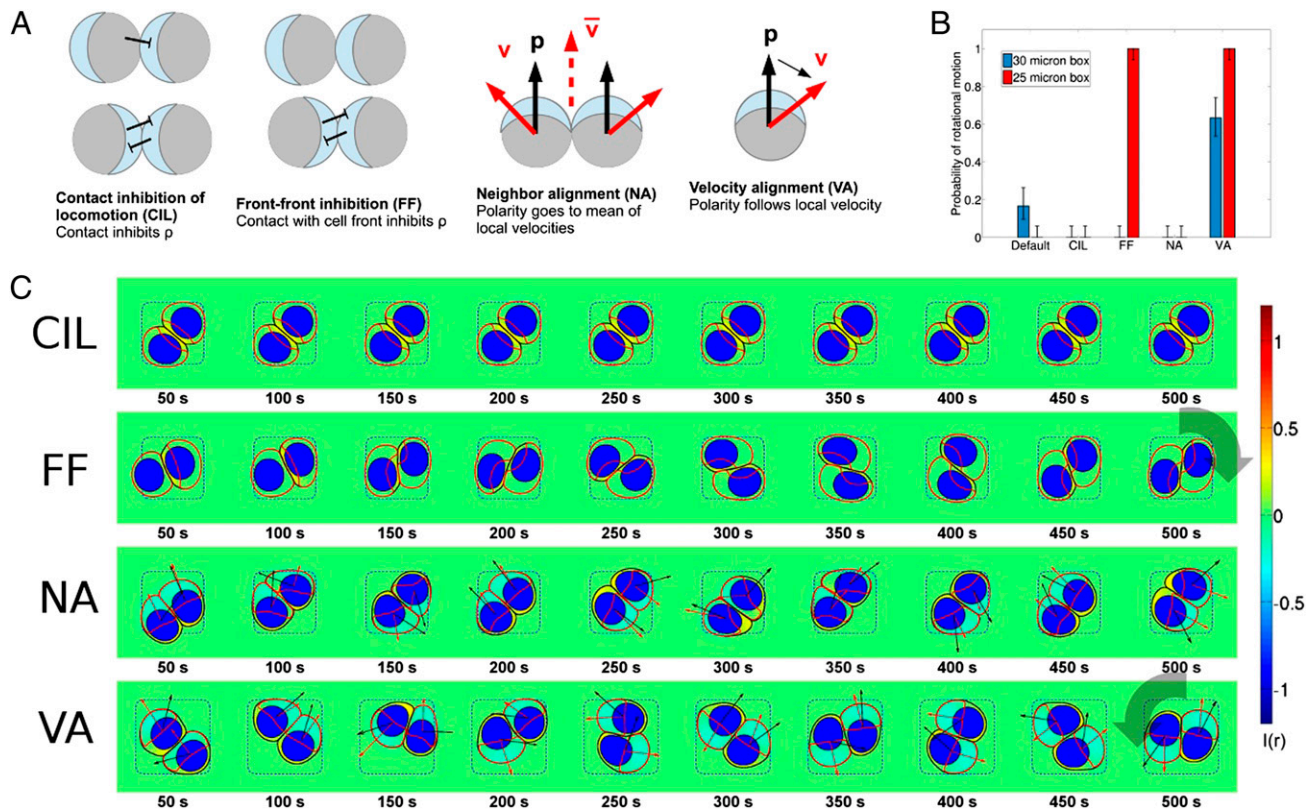


**Fig. 3.** Polarity mechanisms can control persistent rotational motion. (A) We implement four distinct mechanisms for cell polarity. In CIL cell contact locally generates  $I(r)$ , inhibiting  $\rho$ . In FF,  $I(r)$  is generated when a cell contacts another cell's front. Here,  $\rho$  is indicated by light blue at the front of the cell. In the NA and VA mechanisms, we introduce an auxiliary polarity vector  $\hat{p}$  with its own equation of motion. NA orients  $\hat{p}$  to the local average of velocities in its neighborhood  $\bar{v}$  with a timescale  $T_{\text{orient}}$ ; this resembles flocking-inspired models. VA orients  $\hat{p}$  along the cell's velocity with a timescale  $T_{\text{orient}}$ . In both of these models the cell's chemical polarity is then biased to orient the front of the cell (high  $\rho$ ) with the polarity  $\hat{p}$ . There is also a noise term;  $\hat{p}$  fluctuates around its target direction. Details of the implementation of these models are described in *SI Appendix*. (B) PRM probability is controlled by polarity mechanisms; error bars are 68% confidence intervals by the method of ref. 50. "Default" indicates the minimal model with no polarity mechanism. (C) Representative time traces are shown for different polarity mechanisms. Micropattern size  $L_{\text{micro}} = 25 \mu\text{m}$ . As above, cell boundary is shown as a black line,  $\rho(r)$  by its contour (in red), the nucleus by a blue shape, and  $I(r)$  by the color map. In VA and NA mechanisms cell velocity is shown as a red arrow, and the polarity vector  $\hat{p}$  as a black arrow. See also *Movies S3–S11* and *SI Appendix, Fig. S3*.

**Extensions to Different Geometries and Numbers of Cells.** It is straightforward to extend our method to different geometries, simply by changing the function  $\chi(r)$  that describes the adhesive micropattern. It is in principle also simple to increase the number of cells, although the computational expense increases significantly, and smaller time steps may be required to deal with the added extent of cell–cell adhesion. New, more complex dynamics may also appear when the number of cells increases, including changes in cell contact topology (e.g., as studied in ref. 51). We show snapshots of two cells and three cells persistently rotating within circular micropatterns as well as three cells rotating within a square micropattern in *SI Appendix, Fig. S5*.

## Discussion

In our simulation, the shape of the interface between two rotating cells can be strongly influenced by the presence of a nucleus, including changing its chirality (*SI Appendix, Fig. S6*). Huang et al. (20) and Huang and coworkers (21) observed experimentally that, in a pair of rotating cells, the chirality of the cell interface correlates with the direction of the cell motion (fig. 3A in ref. 20). However, the direction of this motion is somewhat counterintuitive (52). If one cell's lamellipodium is pushing on the rear of another cell, it would be natural to assume that the rear of the cell curves inward, but this does not occur. Leong (52) presented a dissipative particle dynamics model of two cells displaying PRM with an interface shape consistent with

experiment. However, this model treats cells as permanently attached to one another and cannot explain how two-cell dynamics arises from single-cell properties. In particular, it is not clear how single-cell persistence appears in Leong's model, or whether an individual cell would develop a polarity. In addition, the model of Leong does not have a nucleus, which may by itself alter the interface curvature. Because interface shape depends on the presence of a nucleus, interface shape may be sensitive to active positioning of the nucleus (53) or rheological details of the cell (54) we have not modeled. Even within our simple model many different parameters, including the micropattern size and the polarity mechanism, may affect the interface shape, and the precise interface shape in PRM is not a robust prediction of our model (*SI Appendix, Fig. S6*), although we expect the influence of the nucleus to remain important. The nuclear effect could be tested by studying PRM of cell types with smaller nuclei or nuclei-free cell fragments (55). PRM in keratocytes and keratocyte fragments may be particularly interesting because our results suggest that even with highly persistent crawling objects, such as keratocytes and fragments, persistent motion may not be robust in the absence of a coordinating mechanism. In addition to the absence of a nucleus, cell–cell adhesion and polarity mechanisms may differ between fragments and keratocytes. If so, keratocytes and keratocyte fragments may differ in both their interface shape and in the robustness of PRM.

Our simulations provide insight into the crucial features regulating the existence and robustness of PRM in cell pairs, which we view as the simplest possible collective motion. Our simulations show that seemingly subtle differences between polarity mechanisms can have significant effects on PRM, and that these differences are robust to changes in many model parameters. The mechanisms of CIL and FF are very similar and may be difficult to distinguish from unconstrained collision data (5). In adhesive stripe assays, collision statistics are simpler to obtain (43, 49); Desai et al. (49) note that head–tail collisions are less likely to lead to repolarization of both cells, consistent with FF rather than our CIL mechanism. However, other mechanisms, such as VA, could also lead to both PRM and asymmetry between head–head and head–tail collisions. These mechanisms may be able to be distinguished using the results of Scarpa et al. (43) and Desai et al. (49). Chiral bias from micropattern shape (56) or intrinsic cell chirality (57) may also be incorporated into our model.

Polarity mechanisms have a strong interplay with confinement. For cells on a 30- $\mu\text{m}$  square, the FF mechanism inhibits PRM, whereas for cells on a 25- $\mu\text{m}$  square FF creates PRM robustly. By contrast, without an explicit polarity mechanism, our model cells cannot polarize on a 25- $\mu\text{m}$  square, and PRM is inhibited. The dependence of cell's ability to polarize on cell size is a feature of the minimal polarity model of Mori et al. (34), and if this model is changed, we would expect details of the polarity–confinement interaction to change. A variety of more complicated and biologically specific polarity models for crawling cells have also been developed (58–62). Many of these models could be implemented within our framework, and we would expect them to alter

the development of PRM to some extent; within recent simulations, the details of the chemical feedbacks alter the ability of the cell to coherently choose a direction when encountering a barrier (62).

The presence or absence of PRM can indicate cell type [endothelial or fibroblast (20), although rotation is seen in larger collections of fibroblasts (57)] or mutation [normal or cancerous (19, 23)]. Huang et al. (20) claim these motions are characteristic of the persistence of the cell motion, and our simulations agree that decreasing cell persistence inhibits PRM. However, we emphasize the role that polarity mechanisms play in coordinating PRM; FF or VA can change our model from displaying 0% PRM to 100% PRM. This suggests that cell polarity mechanism, rather than cell persistence, may distinguish cell types that display PRM and those that do not. Some aspects of CIL are known to differ between normal and malignant cells (63, 64). It may be possible to test the relevant factors by altering cell persistence (65, 66). If the primary regulator of PRM is the cell polarity mechanism, studying PRM provides insight into collective cell migration, where much larger numbers of cells regulate their polarity to move effectively as a group. In particular, our results suggest that contact inhibition of locomotion as modeled here is not a likely cause of collective migration, but that modifications such as front–front inhibition could lead to robust collective motion.

**ACKNOWLEDGMENTS.** B.A.C. thanks Haicen Yue for useful conversations. This work was supported by National Institutes of Health Grants P01 GM078586 and R01 GM096188, National Science Foundation Grants DMS 1309542 and DMS 1319731, and by Center for Theoretical Biological Physics Grant PHY-0822283.

- Friedl P, Gilmour D (2009) Collective cell migration in morphogenesis, regeneration and cancer. *Nat Rev Mol Cell Biol* 10(7):445–457.
- Vedula SR, Ravasio A, Lim CT, Ladoux B (2013) Collective cell migration: A mechanistic perspective. *Physiology (Bethesda)* 28(6):370–379.
- Theveneau E, Mayor R (2013) Collective cell migration of epithelial and mesenchymal cells. *Cell Mol Life Sci* 70:3481–3492.
- Theveneau E, et al. (2010) Collective chemotaxis requires contact-dependent cell polarity. *Dev Cell* 19(1):39–53.
- Carmona-Fontaine C, et al. (2008) Contact inhibition of locomotion in vivo controls neural crest directional migration. *Nature* 456(7224):957–961.
- Weber GF, Bjerke MA, DeSimone DW (2012) A mechanoresponsive cadherin-keratin complex directs polarized protrusive behavior and collective cell migration. *Dev Cell* 22(1):104–115.
- Burak Y, Shraiman BI (2009) Order and stochastic dynamics in Drosophila planar cell polarity. *PLoS Comput Biol* 5(12):e1000628.
- Salbreux G, Barthel LK, Raymond PA, Lubensky DK (2012) Coupling mechanical deformations and planar cell polarity to create regular patterns in the zebrafish retina. *PLoS Comput Biol* 8(8):e1002618.
- Amonlirdviman K, et al. (2005) Mathematical modeling of planar cell polarity to understand domineering nonautonomy. *Science* 307(5708):423–426.
- Vedel S, Tay S, Johnston DM, Bruus H, Quake SR (2013) Migration of cells in a social context. *Proc Natl Acad Sci USA* 110(1):129–134.
- Sepúlveda N, et al. (2013) Collective cell motion in an epithelial sheet can be quantitatively described by a stochastic interacting particle model. *PLoS Comput Biol* 9(3):e1002944.
- Coburn L, Cerone L, Torney C, Couzin ID, Neufeld Z (2013) Tactile interactions lead to coherent motion and enhanced chemotaxis of migrating cells. *Phys Biol* 10(4):046002.
- Szabó B, et al. (2006) Phase transition in the collective migration of tissue cells: Experiment and model. *Phys Rev E Stat Nonlin Soft Matter Phys* 74(6 Pt 1):061908.
- Víček T, Zafeiris A (2012) Collective motion. *Phys Rep* 517(3):71–140.
- Basan M, Elgeti J, Hannezo E, Rappel W-J, Levine H (2013) Alignment of cellular motility forces with tissue flow as a mechanism for efficient wound healing. *Proc Natl Acad Sci USA* 110(7):2452–2459.
- Gov NS (2009) Traction forces during collective cell motion. *HFSP J* 3(4):223–227.
- Kabla AJ (2012) Collective cell migration: Leadership, invasion and segregation. *J R Soc Interface* 9(77):3268–3278.
- Rappel W-J, Nicol A, Sarkissian A, Levine H, Loomis WF (1999) Self-organized vortex state in two-dimensional Dictyostelium dynamics. *Phys Rev Lett* 83(6):1247–1250.
- Doxzen K, Vedula SRK, Leong MC, Hirata H, Gov N, Kabla AJ, Ladoux B, Lim CT (2013) Guidance of collective cell migration by substrate geometry. *Integr Biol* 5:1026–1035.
- Huang S, Brangwynne CP, Parker KK, Ingber DE (2005) Symmetry-breaking in mammalian cell cohort migration during tissue pattern formation: Role of random-walk persistence. *Cell Motil Cytoskeleton* 61(4):201–213.
- Brangwynne C, Huang S, Parker KK, Ingber DE, Ostuni E (2000) Symmetry breaking in cultured mammalian cells. *In Vitro Cell Dev Biol Anim* 36(9):563–565.
- Angelini TE, et al. (2011) Glass-like dynamics of collective cell migration. *Proc Natl Acad Sci USA* 108(12):4714–4719.
- Tanner K, Mori H, Mroue R, Bruni-Cardoso A, Bissell MJ (2012) Coherent angular motion in the establishment of multicellular architecture of glandular tissues. *Proc Natl Acad Sci USA* 109(6):1973–1978.
- Rorth P (2012) Fellow travellers: Emergent properties of collective cell migration. *EMBO Rep* 13(11):984–991.
- Shao D, Rappel W-J, Levine H (2010) Computational model for cell morphodynamics. *Phys Rev Lett* 105(10):108104.
- Kockelkoren J, Levine H, Rappel W-J (2003) Computational approach for modeling intra- and extracellular dynamics. *Phys Rev E Stat Nonlin Soft Matter Phys* 68(3 Pt 2):037702.
- Boettinger WJ, Warren JA, Beckermann C, Karma A (2002) Phase-field simulation of solidification 1. *Annu Rev Mater Res* 32(1):163–194.
- Collins JB, Levine H (1985) Diffuse interface model of diffusion-limited crystal growth. *Phys Rev B Condens Matter* 31(9):6119–6122.
- Ziebert F, Swaminathan S, Aranson IS (2012) Model for self-polarization and motility of keratocyte fragments. *J R Soc Interface* 9(70):1084–1092.
- Li X, Lowengrub J, Rätz A, Voigt A (2009) Solving PDEs in complex geometries: A diffuse domain approach. *Commun Math Sci* 7(1):81–107.
- Marth W, Voigt A (2013) Signaling networks and cell motility: A computational approach using a phase field description. *J Math Biol* 69(1):91–112.
- Shao D, Levine H, Rappel W-J (2012) Coupling actin flow, adhesion, and morphology in a computational cell motility model. *Proc Natl Acad Sci USA* 109(18):6851–6856.
- Camley BA, Zhao Y, Li B, Levine H, Rappel WJ (2013) Periodic migration in a physical model of cells on micropatterns. *Phys Rev Lett* 111(15):158102.
- Mori Y, Jilkine A, Edelstein-Keshet L (2008) Wave-pinning and cell polarity from a bistable reaction-diffusion system. *Biophys J* 94(9):3684–3697.
- Albert PJ, Schwarz US (2014) Dynamics of cell shape and forces on micropatterned substrates predicted by a cellular Potts model. *Biophys J* 106(11):2340–2352.
- Helfrich W (1973) Elastic properties of lipid bilayers: Theory and possible experiments. *Z Naturforsch C* 28(11):693–703.
- Canham PB (1970) The minimum energy of bending as a possible explanation of the biconcave shape of the human red blood cell. *J Theor Biol* 26(1):61–81.
- Li B, Zhao Y (2013) Variational implicit solvation with solute molecular mechanics: from diffuse-interface to sharp-interface models. *SIAM J Appl Math* 73(1):1–23.
- Röger M, Schätzle R (2006) On a modified conjecture of De Giorgi. *Math Z* 254(4):675–714.
- Nonomura M (2012) Study on multicellular systems using a phase field model. *PLoS ONE* 7(4):e33501.
- Doyle AD, Wang FW, Matsumoto K, Yamada KM (2009) One-dimensional topography underlies three-dimensional fibrillar cell migration. *J Cell Biol* 184(4):481–490.
- Mori Y, Jilkine A, Edelstein-Keshet L (2011) Asymptotic and bifurcation analysis of wave-pinning in a reaction-diffusion model for cell polarization. *SIAM J Appl Math* 71(4):1401–1427.



# Polarity mechanisms such as contact inhibition of locomotion regulate persistent rotational motion of mammalian cells on micropatterns: SI Text

Brian A. Camley      Yunsong Zhang      Yanxiang Zhao      Bo Li      Eshel Ben-Jacob  
 Herbert Levine      Wouter-Jan Rappel

## 1 Elements of the model and figure interpretation

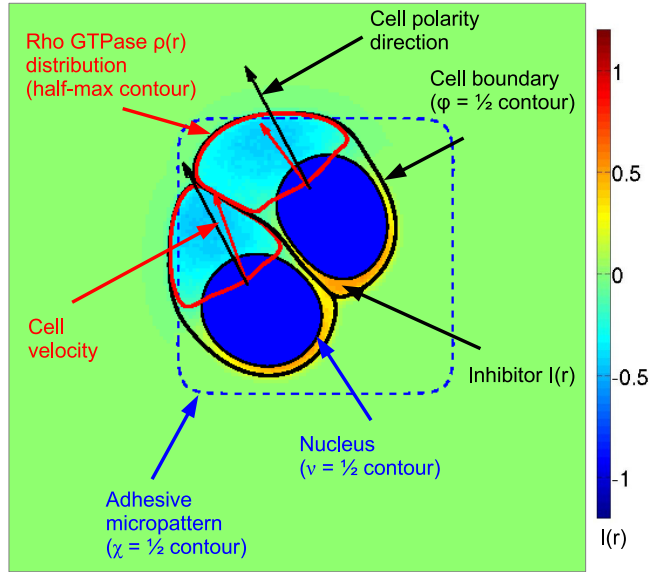


Figure S1: **Elements of model.** We track our cell’s shape by a phase field  $\phi(\mathbf{r})$ ; its boundary is plotted as a black line at the  $\phi(\mathbf{r}) = 1/2$  contour. To show the cell front, where the Rho GTPase  $\rho(\mathbf{r})$  is high, we plot the half-maximum contour of  $\rho\phi$  in red. We show the nucleus in solid blue (its boundary is set by  $\nu(\mathbf{r}) = 1/2$ ). The fluctuating inhibitor field  $I(\mathbf{r})$  is shown as a color map ( $I(\mathbf{r})\phi(\mathbf{r})$  is plotted to restrict  $I$  to the interior of the cell), with the color scale indicated to the right; all of our figures use this color scale for  $I(\mathbf{r})$ . We have also indicated the adhesive micropattern region; this is static, but indicated by a field  $\chi(\mathbf{r})$ . In some of our simulations, we will include an internal polarity vector for each cell, which will be plotted as a black vector. We have also plotted here the cell’s center of mass velocity as a red vector.

## 2 Derivation of phase field equations from force balance

We briefly review the phase field method of tracking a cell boundary as developed in [1]. We assume that the cell interface motion is local and overdamped, i.e. that the interface velocity is directly proportional to the force applied to the interface:

$$\mathbf{v}_{\text{int}} = \frac{1}{\tau} \mathbf{F}_{\text{int}} \quad (\text{S1})$$

where  $\tau$  describes the frictional drag between the cell and substrate. The force  $\mathbf{F}_{\text{int}}$  is the force per unit length. This is the same as arguing that the interface force is balanced by a frictional drag  $\mathbf{F}_{\text{drag}} = -\tau \mathbf{v}_{\text{int}}$ , with  $\mathbf{F}_{\text{int}} + \mathbf{F}_{\text{drag}} = 0$ . The boundary of the cell is tracked by a phase field  $\phi(\mathbf{r}, t)$ , which smoothly approaches zero outside the cell and approaches unity within it; the cell boundary is set implicitly by  $\phi = 1/2$ . We track the interface using the advection scheme:

$$\partial_t \phi + \mathbf{v}_{\text{int}} \cdot \nabla \phi = 0. \quad (\text{S2})$$

The cell motion will depend on the origins of the force  $\mathbf{F}_{\text{int}}$ . In Shao et al. [1] there are three components to the force: 1) membrane tension and bending forces, derived from a Hamiltonian, 2) active forces arising from actin-based protrusion

and myosin-based contraction, and 3) a constraint force keeping the cell area fixed,  $\mathbf{F}_{\text{int}} = \mathbf{F}_{\text{H}} + \mathbf{F}_{\text{active}} + \mathbf{F}_{\text{area}}$ . Since we are including the possibility of cell spreading, we will not keep the cell area fixed in this work, though we will use a similar force to keep the cell's nuclear area constant. In addition, we will include terms in the Hamiltonian beyond the membrane deformations, including cell-cell adhesion and exclusion. We will not need to specify the Hamiltonian to derive the phase-field equations.

If  $\phi(\mathbf{r})$  is not given by the energy-minimizing state  $\frac{\delta H}{\delta \phi} = 0$ , we can write down the induced force density [2, 3]

$$\mathbf{F}_{\text{H}}^*(\mathbf{r}) = \frac{\delta H}{\delta \phi} \nabla \phi. \quad (\text{S3})$$

To convert between a two-dimensional force density  $\mathbf{F}^*$  and its corresponding interfacial force  $\mathbf{F}$  as used in Eq.S1, we use a function  $\delta_\epsilon(\mathbf{r}) = \epsilon |\nabla \phi|^2$  which indicates the interface. We then write

$$\mathbf{F}^* d^2 r = \mathbf{F} dl = \mathbf{F} \delta_\epsilon(\mathbf{r}) d^2 r \quad (\text{S4})$$

e.g.  $\mathbf{F}_{\text{H}} = \mathbf{F}_{\text{H}}^*/\delta_\epsilon(\mathbf{r})$ .

We use a simple form for the active forces at the membrane's surface, setting (in the absence of any micropattern)

$$\mathbf{F}_{\text{active}} = (\alpha \rho - \beta) \hat{\mathbf{n}} \quad (\text{S5})$$

where  $\rho$  is the concentration of actin promoter within the cell and  $\hat{\mathbf{n}} = -\frac{\nabla \phi}{|\nabla \phi|}$  is the outward-pointing normal to the cell surface. Similar choices are used in [1,4]. Under this minimal rule, the area of the cell where  $\rho$  is high will be pushed outward, and the back of the cell where  $\rho$  is low (smaller than  $\beta/\alpha$ ) will be pulled in.

Combining these results, we can write  $\mathbf{v}_{\text{int}}$  in terms of the fields  $\phi$  and  $\rho$ , and our equation of motion for  $\phi(\mathbf{r}, t)$  (Eq.S2) becomes

$$\partial_t \phi(\mathbf{r}, t) = \frac{1}{\tau} (\alpha \rho - \beta) |\nabla \phi| - \frac{1}{\tau \epsilon} \frac{\delta H}{\delta \phi}. \quad (\text{S6})$$

## 2.1 Inclusion of cell nucleus

We treat the cell nucleus using a second phase field,  $\nu(\mathbf{r}, t)$ . This nucleus is modeled as an object with a fixed line tension  $\gamma_{\text{nuc}}$  and bending modulus  $\kappa_{\text{nuc}}$ , as well as an area constraint fixing its area to  $A_{\text{nuc}} = \pi R_{\text{nuc}}^2$ . We implement this area constraint as an isotropic penalty force, as in [1]

$$\mathbf{F}_{\text{area}} = -M (A_\nu - A_{\text{nuc}}) \hat{\mathbf{n}}_\nu \quad (\text{S7})$$

where  $A_\nu = \int d^2 r \nu(\mathbf{r})$ ;  $M$  is a multiplier chosen to be large enough to keep the nuclear area roughly fixed, and  $\hat{\mathbf{n}}_\nu = -\frac{\nabla \nu}{|\nabla \nu|}$  is the outward-pointing normal to the nucleus surface. The equation for the nucleus phase field  $\nu(\mathbf{r}, t)$  becomes

$$\partial_t \nu(\mathbf{r}, t) = -\frac{M}{\tau_{\text{nuc}}} (A_\nu - A_{\text{nuc}}) |\nabla \nu| - \frac{1}{\tau_{\text{nuc}} \epsilon} \frac{\delta H}{\delta \nu} \quad (\text{S8})$$

where  $\tau_{\text{nuc}}$  is the nuclear equivalent of  $\tau$ , a friction coefficient relating the velocity of the nucleus' boundary to the forces applied to it. We note that we have allowed  $\tau_{\text{nuc}}$  to differ from  $\tau$ ; this term reflects the friction on the nucleus. If  $\tau_{\text{nuc}}$  is increased, the cell will eventually be unable to pull the nucleus.

The generalization to many cells, which is presented explicitly in the main paper, is straightforward.

## 2.2 Effect of micropattern on cell dynamics

We model the micropattern with an approach similar to the one we used in [5]. We represent the micropattern by a normalized ligand density  $\chi(\mathbf{r})$ , and restrict protrusion to occur only on the micropattern, i.e. we set  $\mathbf{F}_{\text{active}} = [\alpha \chi(\mathbf{r}) \rho - \beta] \hat{\mathbf{n}}$ . This models the cell as unable to generate pushing forces without the adhesion between the cell and substrate. We then have a phase field equation of the form

$$\partial_t \phi(\mathbf{r}, t) = \frac{1}{\tau} [\alpha \chi(\mathbf{r}) \rho - \beta] |\nabla \phi| - \frac{1}{\tau \epsilon} \frac{\delta H}{\delta \phi}. \quad (\text{S9})$$

To model a smooth profile of ligand, we choose the form

$$\chi(\mathbf{r}) = \frac{1}{16} \left[ 1 + \tanh \left( \frac{L_{\text{micro}}/2 - x}{\epsilon} \right) \right] \left[ 1 + \tanh \left( \frac{L_{\text{micro}}/2 - y}{\epsilon} \right) \right] \times \left[ 1 + \tanh \left( \frac{x + L_{\text{micro}}/2}{\epsilon} \right) \right] \left[ 1 + \tanh \left( \frac{y + L_{\text{micro}}/2}{\epsilon} \right) \right] \quad (\text{S10})$$

which describes an adhesive square of size  $L_{\text{micro}} \times L_{\text{micro}}$ . Other micropattern shapes can be very simply generated by choosing a different form for  $\chi(\mathbf{r})$ ; we show an example of cell dynamics on a circular micropattern in Fig.S5.

### 3 Reaction-diffusion mechanisms within the cell: reaction terms $f_\rho$ and $f_I$

#### 3.1 $\rho(\mathbf{r})$ dynamics: cell front-back polarity

We describe the dynamics of the cell's chemical polarization using a variant of the reaction-diffusion model first proposed by Mori et al. [6]. This model describes the dynamics of a Rho GTPase that defines the front of the cell, e.g. Rac or cdc42. In this model, the Rho GTPase may move between membrane-bound ( $\rho(\mathbf{r}, t)$ ) and cytosolic ( $\rho_{\text{cyt}}$ ) states. The membrane-bound state recruits  $\rho$  from the cytoplasm, but the total number  $N_{\text{tot}}$  of Rho GTPase molecules is conserved. We assume that the cytoplasmic Rho GTPase  $\rho_{\text{cyt}}$  is well-mixed (i.e. constant) over the time scales studied, while  $\rho$  diffuses with a diffusion coefficient  $D_\rho$ . This model robustly produces a well-defined “front” (high  $\rho$ ) and “back” (low  $\rho$ ) to the cell.

This reaction-diffusion model has a reaction term  $f_\rho(\rho, \rho_{\text{cyt}}, I)$  where

$$f_\rho(\rho, \rho_{\text{cyt}}, I) = k_b \left( \frac{\rho^2}{K_a^2 + \rho^2} + k_a \right) \rho_{\text{cyt}} - k_c [1 + I(\mathbf{r})] \rho. \quad (\text{S11})$$

As described above, this reaction term includes a transition from membrane-bound to cytosolic state with reaction rate constant  $k_c(1+I)$  (i.e. positive  $I$  increases the rate of transition  $\rho \rightarrow \rho_{\text{cyt}}$ ), a first-order rate from cytosolic to membrane-bound ( $k_a k_b$ ), and a nonlinear term describing recruitment. The total amount of  $\rho$  is conserved,  $\int d^2r (\rho(\mathbf{r}) + \rho_{\text{cyt}}) \phi(\mathbf{r}) = N_{\text{tot}}$ . We assume that the cytosolic actin promoter is well-mixed (uniform), so  $\rho_{\text{cyt}}$  is “slaved” to  $\rho$ :

$$\rho_{\text{cyt}} = \frac{N_{\text{tot}} - \int d^2r \rho(\mathbf{r}) \phi(\mathbf{r})}{\int d^2r \phi(\mathbf{r})}. \quad (\text{S12})$$

#### 3.2 $I(\mathbf{r})$ dynamics: calibrating persistence of single model cells

As discussed in the main text, we introduce a fluctuating field  $I(\mathbf{r})$  to control the cell's persistence, i.e. the time over which the cell's direction and velocity are maintained. We also use this field to describe polarity mechanisms. This field has a reaction term

$$f_I(I, \{\phi\}) = -k_{-I}I + \xi(\mathbf{r}, t) + \text{polarity mechanism terms}. \quad (\text{S13})$$

$\xi(\mathbf{r}, t)$  is a Gaussian Langevin noise with zero mean and a variance

$$\langle \xi(\mathbf{r}, t) \xi(\mathbf{r}', t') \rangle = \eta^2 \delta^2(\mathbf{r} - \mathbf{r}') \delta(t - t'). \quad (\text{S14})$$

In practice, when we numerically solve the reaction-diffusion equations, we will represent the Dirac delta function above as a Gaussian random variable that is uncorrelated between lattice sites, but with a variance rescaled by  $\Delta x^{-2}$ ; this is required to ensure that the noise amplitude will not change if the resolution changes (numerical details in Section 13).

We note that earlier models exist for the description of cell protrusions and polarity; many of these are reviewed in [7–9]. We have chosen the mechanism here for its relative simplicity, and because it reduces easily to a steadily-crawling model in the limit  $\eta \rightarrow 0$ .

We systematically vary the noise strength  $\eta$  and measure its effect on the center of mass motion of the cell (Fig.S2). As the units of  $\eta^2$  are  $\mu m^2/s$ , we will instead report  $\bar{\eta}^2 = \eta^2/D_I$ , which is unitless. We measure the velocity-velocity correlation of the cell center of mass,  $\mathbf{R}_{\text{cm}}$ ,

$$\mathbf{R}_{\text{cm}} \equiv \frac{\int d^2r \mathbf{r} \phi(\mathbf{r})}{\int d^2r \phi(\mathbf{r})} \quad (\text{S15})$$

and  $\mathbf{v}_{\text{cm}} = \frac{d}{dt} \mathbf{R}_{\text{cm}}$ . We define  $t_{1/2}$  as the time at which the relevant normalized velocity-velocity correlation function reaches 1/2, i.e.

$$C_{vv}(t_{1/2}) = \frac{\langle \mathbf{v}_{\text{cm}}(t + t_{1/2}) \cdot \mathbf{v}_{\text{cm}}(t) \rangle}{\langle |\mathbf{v}_{\text{cm}}|^2 \rangle} = \frac{1}{2}. \quad (\text{S16})$$

We find that the persistence time  $t_{1/2}$  of the cell center of mass increase sharply as  $\bar{\eta}$  is decreased to zero (Fig.S2). These results are for the reaction term above, with no polarity mechanism assumed; if a VA or NA mechanism is applied, this may potentially change the cell persistence.

### 4 The cell-cell adhesion force: what does $\sigma$ mean?

The cell-cell adhesion term is given by

$$H_{\text{adhesion}} = - \sum_{i \neq j} \int d^2r \frac{\sigma \epsilon^3}{4} |\nabla \phi^{(i)}|^2 |\nabla \phi^{(j)}|^2. \quad (\text{S17})$$

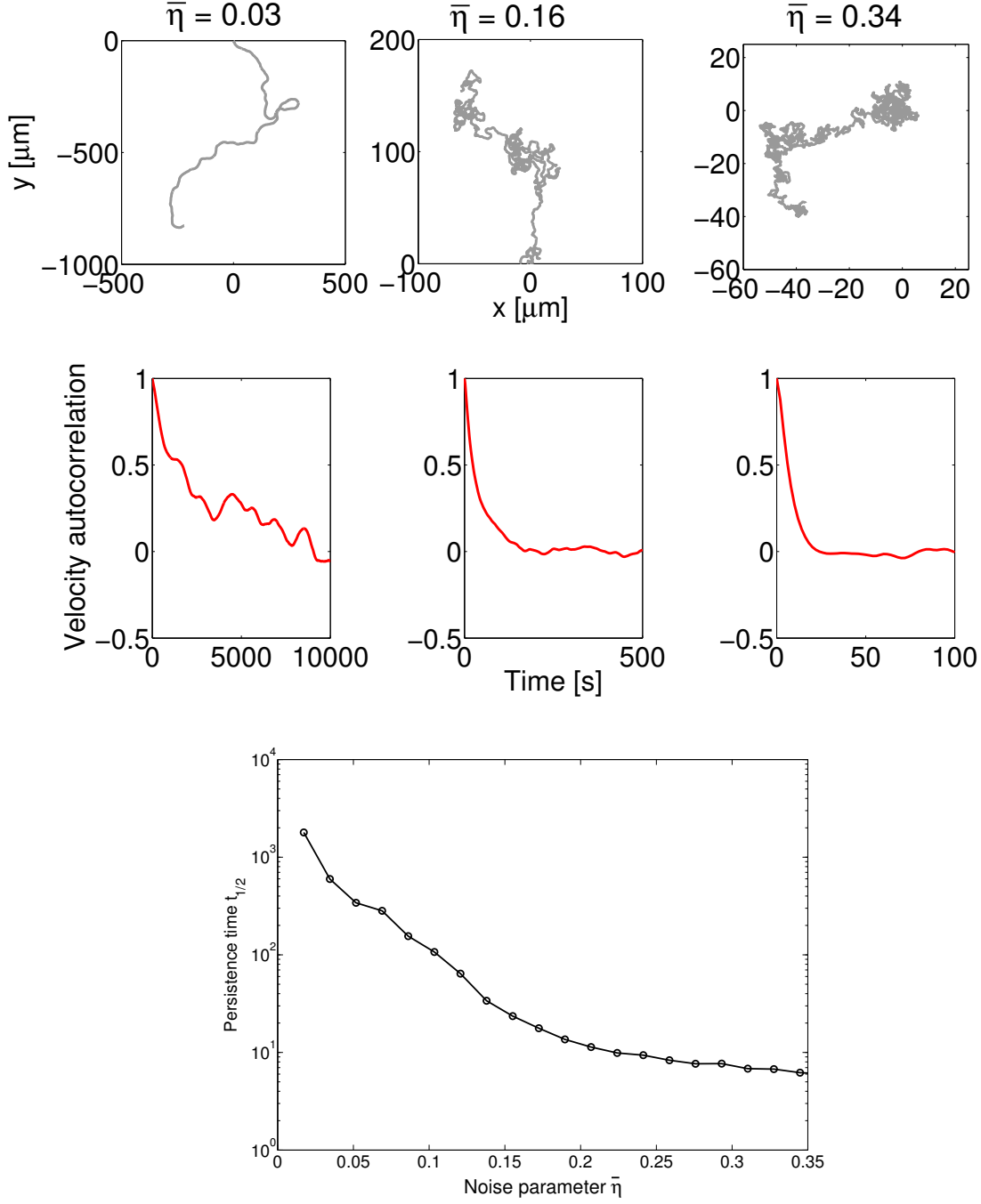


Figure S2: **Changing inhibitor noise  $\bar{\eta}$  changes cell persistence.** We show how single-cell trajectories (first row) and normalized velocity autocorrelation functions (second row) change as a function of the inhibitor noise  $\bar{\eta}$  (where  $\bar{\eta}^2 = \eta^2/D_I$ ). We can characterize this general behavior by looking at the persistence time  $t_{1/2}$ . We define  $t_{1/2}$  as the time at which the normalized velocity-velocity correlation function reaches 1/2, i.e.  $\langle \mathbf{v}(t + t_{1/2}) \cdot \mathbf{v}(t) \rangle = \frac{1}{2} \langle |\mathbf{v}|^2 \rangle$ . These single-cell simulations are performed with a larger time step of  $\Delta t = 0.005$ . Trajectories are plotted for times of 20,000 seconds, 20,000 seconds, and 15,000 seconds for  $\bar{\eta} = 0.03, 0.16$ , and  $0.34$  respectively; this is also the data used to create the velocity-velocity autocorrelations.

The sum  $\sum_{i \neq j}$  is a sum over  $i$  and  $j$  from 1 to  $n_c$ , excepting only  $i = j$  – we note that each cell pair is counted twice in this sum in our convention.  $\sigma$  sets the scale of the energy of adhesion; it has units of energy per unit length. However,  $\sigma$  is not a numerically precise energy of adhesion per length of overlap. We consider two perfectly overlapping interfaces that minimize the Helfrich energy ( $H_\phi$ ),  $\phi^{(1)} = \frac{1}{2}(1 + \tanh \frac{3x}{\epsilon})$  and  $\phi^{(2)} = \frac{1}{2}(1 - \tanh \frac{3x}{\epsilon})$ . For a fixed length  $L$  in the  $y$  direction, we find  $H_{\text{adhesion}} = -\sigma L \frac{27}{32} \int_{-\infty}^{\infty} du \operatorname{sech}^8 u = -\frac{27}{35} \sigma L$ ; the effective adhesion energy per overlapping length is  $\frac{27}{35} \sigma \approx 0.77\sigma$ . If the interfaces are curved, or otherwise distorted (e.g. by the cell-cell repulsion), this result may also be quantitatively altered.

#### 4.1 A note on the sharp-interface limit

The quantitative application of phase field methods is often made more difficult by the need to reach a sharp interface limit,  $\epsilon \rightarrow 0$  (see, e.g. Ref. [10] and references within). Because our focus in this work is not quantitative comparisons, we will not explicitly study this aspect. However, we should note that our approach (and the related one of Nonomura [11]) raise interesting questions about the sharp interface limit of the adhesion terms proposed phenomenologically here. In the limit  $\epsilon \rightarrow 0$ , what does Eq.S17 mean? Our simple argument above suggests that it corresponds to an energy of  $-\frac{27}{35}\sigma$  per unit length of overlapping edge – but the meaning of “overlapping” in a sharp interface sense may not be clear.

Attempts to refine our calculations for  $\epsilon \rightarrow 0$  would also need to address the sharp-interface limit of the cell-cell interactions in polarity mechanisms, as described in Section 6.

### 5 Initial conditions

In our multiple-cell simulations, we initiate the cells with different positions as well as different random initial distributions of  $\rho(\mathbf{r})$ . We choose the initial centers of the cells with a uniform distribution over the square micropattern  $-L_{\text{micro}}/2 \leq x \leq L_{\text{micro}}/2, -L_{\text{micro}}/2 \leq y \leq L_{\text{micro}}/2$ , excluding only those configurations where the cell centers are within  $0.3R_{\text{cell}}$  of each other. This includes cases with some initial overlap – the cells quickly move and deform to eliminate this overlap. We choose an initial cell size of  $R_{\text{cell}} = 10 \mu\text{m}$ , which we implement as an initial  $\phi$  field  $\phi(\mathbf{r}) = \frac{1}{2} + \frac{1}{2} \tanh [3(R_{\text{cell}} - r)/\epsilon]$ , where  $r$  indicates the distance from the chosen center of mass. (An equivalent choice is made for the initial value of  $\nu(\mathbf{r})$ , but with the nuclear radius  $R_{\text{nuc}}$ ). The  $\rho$  distribution is initialized to a uniform value with a large noise, leading the cells to spontaneously develop a polarity. This distribution for  $\rho$  is  $\max(1.8 + \text{noise}, 0) \mu\text{m}^{-2}$  where the noise is normally-distributed at each lattice point with a standard deviation of  $1.8\mu\text{m}^{-2}$ . Initially,  $I(\mathbf{r})$  is set to zero everywhere.

### 6 Implementing polarity mechanisms in a phase field model

We can use our combined mechanical and chemical model as a platform to implement several potential mechanisms to determine the in-plane polarity of our cells. These polarity mechanisms are contact inhibition of locomotion (CIL), front-front inhibition (FF), neighbor alignment (NA), and velocity alignment (VA).

#### 6.1 Contact inhibition of locomotion (CIL)

To model contact inhibition of locomotion (CIL), we generate the inhibitor  $I$  in cells where they contact their neighbors; neighbor contact is indicated by the nonzero value of a phase field other than the cell’s. We modify the reaction term  $f_I$ ,

$$f_I^{\text{CIL}}[I^{(i)}, \{\phi\}] = k_I S \left( \sum_{j \neq i} \phi^{(j)} \right) - k_{-I} I^{(i)} + \xi^{(i)}(\mathbf{r}, t) \quad (\text{S18})$$

where  $S(x) = \max(0, \tanh[x/x_0])$ . Here,  $k_I$  controls the strength of the generation of inhibitor, and the form of  $S(x)$  is chosen to saturate, so that large overlaps between cells do not generate huge amounts of  $I$ ; we choose  $x_0 = 0.1$  throughout this paper.

#### 6.2 Front-front inhibition (FF)

We generalize the idea of contact inhibition of locomotion to the case where only contact with the front of the cell ( $\rho$  large) leads to inhibition:

$$f_I^{\text{FF}}[I^{(i)}, \{\phi\}, \{\rho\}] = k_I S \left( \frac{\sum_{j \neq i} \rho^{(j)} \phi^{(j)}}{\rho^{\text{char}}} \right) - k_{-I} I^{(i)} + \xi^{(i)}(\mathbf{r}, t) \quad (\text{S19})$$

where  $S(x) = \max(0, \tanh[x/x_0])$ ,  $x_0 = 0.1$  as above, and we set  $\rho^{\text{char}} = 1\mu\text{m}^{-2}$ . This characteristic scale is smaller than the typical value of  $\rho$  at the cell front, which is usually around  $1.4\mu\text{m}^{-2}$ , but is much larger than the value at the back, which is typically around  $0.01\mu\text{m}^{-2}$ .

### 6.3 Velocity-alignment of polarity (VA)

We introduce a unit vector for each cell to track the cell's targeted polarity,  $\hat{\mathbf{p}}^{(i)} \equiv (\cos \theta^{(i)}, \sin \theta^{(i)})$ . This additional polarity vector has its own dynamics. For the VA model, we follow [12–14] in aligning the polarity of the cell with its velocity. We write the dynamics of  $\hat{\mathbf{p}}^{(i)}$  as

$$\partial_t \theta^{(i)} = \frac{1}{T_{\text{orient}}} \arcsin \left[ \cos \theta^{(i)} \sin \theta_v^{(i)} - \sin \theta^{(i)} \cos \theta_v^{(i)} \right] + \zeta z(t) \quad (\text{S20})$$

where  $\theta_v^{(i)} = \arg \mathbf{v}_{\text{cm}}^{(i)}$  is the angle of the cell's center-of-mass velocity and  $z(t)$  is a Gaussian Langevin noise with unit variance,  $\langle z(t)z(t') \rangle = \delta(t-t')$ . This form is the one suggested originally by Szabo et al. [12]; it is an appropriate periodic extension of writing  $-\frac{1}{T_{\text{orient}}} (\theta^{(i)} - \theta_v)$  [15]. Note that  $\arcsin \left[ \cos \theta^{(i)} \sin \theta_v^{(i)} - \sin \theta^{(i)} \cos \theta_v^{(i)} \right] = \arcsin \left[ -\sin \left( \theta^{(i)} - \theta_v^{(i)} \right) \right] = -\left( \theta^{(i)} - \theta_v^{(i)} \right)$ , where the last equality holds when  $|\theta^{(i)} - \theta_v^{(i)}| \leq \pi/2$ .

In order to make the Rho GTPase align with our new polarity vector  $\hat{\mathbf{p}}^{(i)}$ , we modify the reaction kinetics of the inhibitor  $I$ :

$$f_I^{\text{pol}}[I^{(i)}, \{\phi\}] = -k_I \hat{\mathbf{p}}^{(i)} \cdot \left( \frac{\mathbf{r} - \mathbf{R}_{\text{cm}}^{(i)}}{|\mathbf{r} - \mathbf{R}_{\text{cm}}^{(i)}|} \right) - k_{-I} I^{(i)} + \xi^{(i)}(\mathbf{r}, t) \quad (\text{S21})$$

where the center of mass of cell  $i$  is given by

$$\mathbf{R}_{\text{cm}}^{(i)} = \frac{\int d^2 r \mathbf{r} \phi^{(i)}(\mathbf{r})}{\int d^2 r \phi^{(i)}(\mathbf{r})}. \quad (\text{S22})$$

We note that though  $\zeta$  is large and the polarity fluctuates strongly around the velocity, the orientational persistence time  $t_{1/2}$  of a single VA cell (around 1300 seconds with default parameters) remains comparable to that of a single CIL or FF cell (around 1700 s); if  $\zeta$  is set to zero, a VA cell has a significantly larger persistence time than a FF cell.

### 6.4 Neighbor-alignment of velocities (NA)

To model alignment between neighboring cells, we use the scheme from the previous section, including Eq.S21, but alter the dynamics of the polarity vector  $\hat{\mathbf{p}}^{(i)}$ . We choose, similarly to the VA model,

$$\partial_t \theta^{(i)} = \frac{1}{T_{\text{orient}}} \arcsin \left[ \cos \theta^{(i)} \sin \theta_{\bar{v}} - \sin \theta^{(i)} \cos \theta_{\bar{v}} \right] + \zeta z(t) \quad (\text{S23})$$

where  $z(t)$  is a Langevin noise as above,  $\theta_{\bar{v}} = \arg \bar{\mathbf{v}}_{\text{cm}}$ , and  $\bar{\mathbf{v}}_{\text{cm}}$  is the mean velocity of all cells in our system, where  $\mathbf{v}_{\text{cm}}^{(i)} = \frac{d}{dt} \mathbf{R}_{\text{cm}}^{(i)}$ . In simulations of larger collections of cells, a cutoff distance is usually applied for this alignment interaction [16]; in our model, we assume that this cutoff distance is larger than the micropattern.

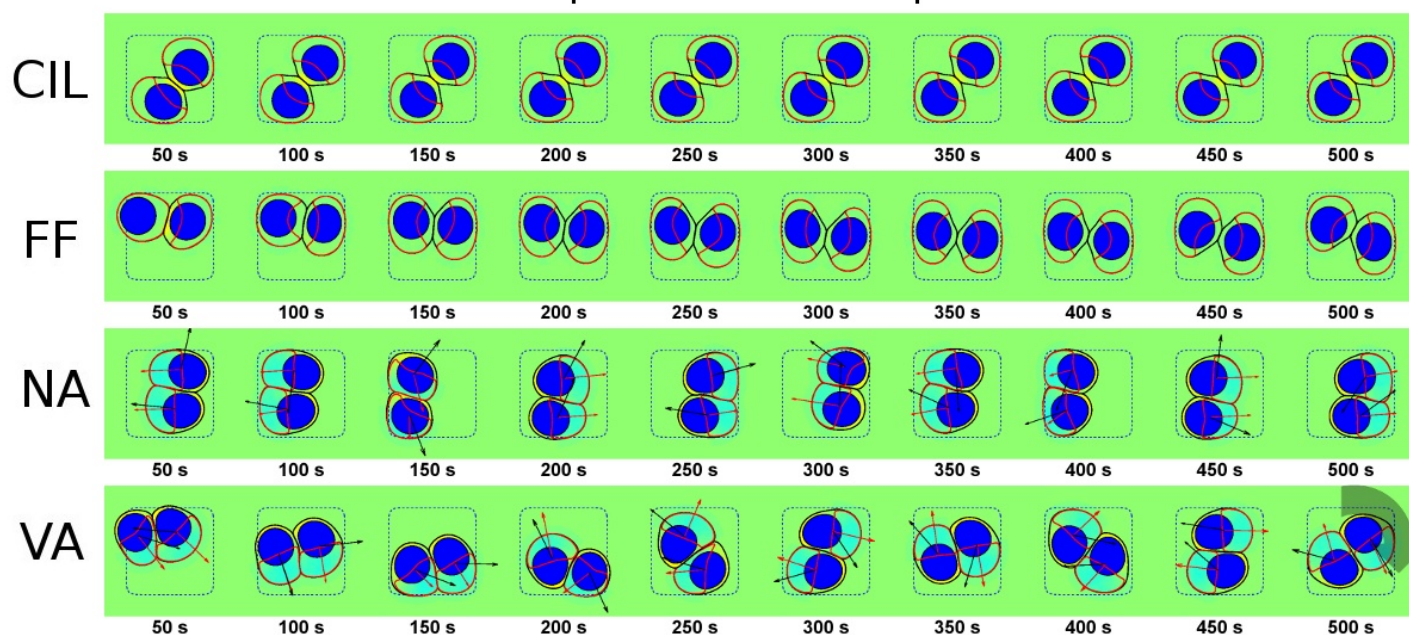
## 7 Effect of polarity mechanisms in $L_{\text{micro}} = 30 \mu\text{m}$ micropattern

We have shown typical simulations of PRM in micropatterns of size  $L_{\text{micro}} = 25 \mu\text{m}$  in the main paper. We compare these results to simulations in  $L_{\text{micro}} = 30 \mu\text{m}$  micropatterns in Fig.S3. The primary effect of increasing micropattern size is to disrupt PRM for FF cells.

## 8 Cell rotational motion is disrupted in cells with lower persistence

We have shown that the presence and robustness of persistent rotational motion can be controlled by polarity alignment mechanisms. However, persistent rotational motion also requires that the cell's linear motion be sufficiently persistent; as the model of Huang et al. [17] makes clear, cells that undergo effectively pure random-walk motility are not likely to develop rotation. In our model, the persistence time (as measured from the cell's velocity-velocity correlation function) is controlled by the amplitude of the fluctuating source term in the  $I(\mathbf{r})$  equation (see Fig.S2). In Fig.S4, we vary this amplitude,  $\bar{\eta}$ , and show that the presence of persistent rotation is disrupted at large  $\bar{\eta}$ . The simulations presented in Fig.S4 use the FF mechanism in a  $25 \mu\text{m}$  micropattern, which robustly generates PRM for highly persistent cells ( $\bar{\eta} = 0.03$ ). Decreasing persistence can lead to transient reversals, as well as complete elimination of rotation in some cases. We do not perform a similar analysis for the velocity-alignment mechanism, as VA cells will have a different calibration between persistence time and the noise  $\bar{\eta}$  and the noise strength  $\zeta$ .

Micropattern size = 30  $\mu\text{m}$



Micropattern size = 25  $\mu\text{m}$

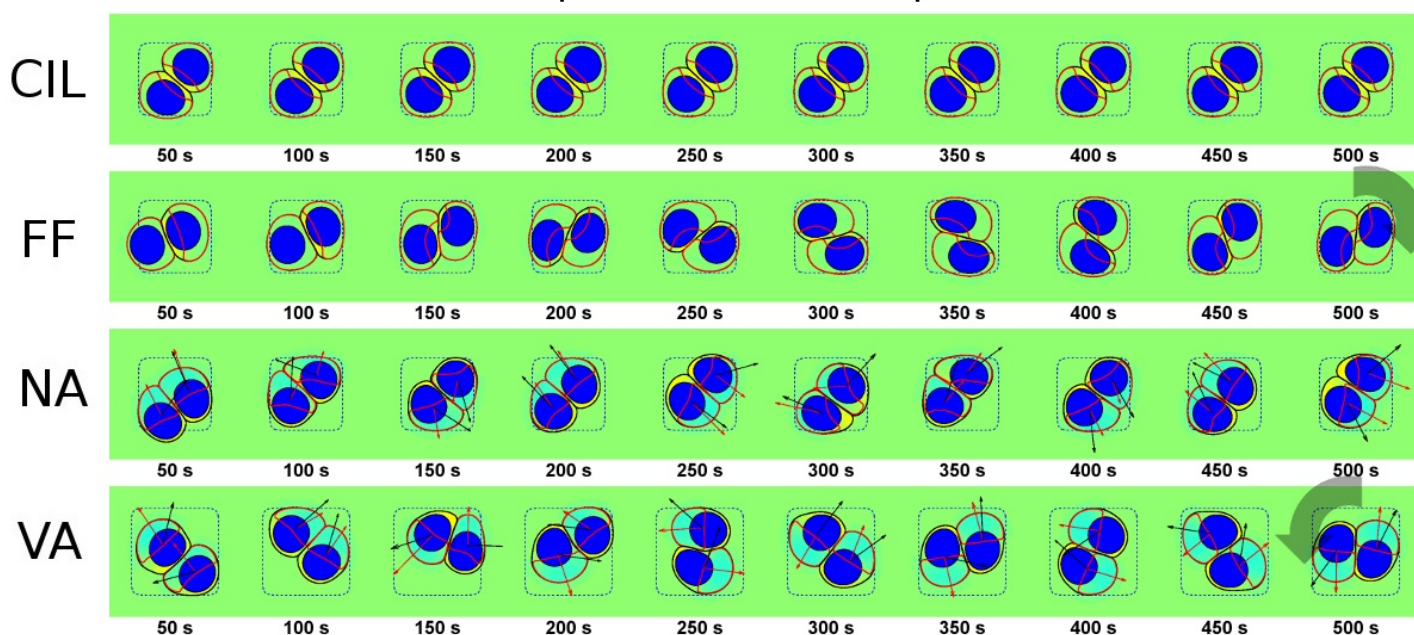


Figure S3: **Polarity mechanisms can control persistent rotational motion, but interacts with micropattern size.** Representative time traces are shown for different polarity mechanisms. TOP: Micropattern size  $L_{\text{micro}} = 30 \mu\text{m}$ ; BOTTOM: Micropattern size  $L_{\text{micro}} = 25 \mu\text{m}$  (This figure is repeated from the main text for comparison). See also Supplementary Movies S3-S11.

## 9 Extensions to different geometries and numbers of cells

It is straightforward to extend our method to different geometries, simply by changing the function  $\chi(\mathbf{r})$  that describes the adhesive micropattern. It is in principle also simple to increase the number of cells, though the computational expense increases, and smaller time steps may be required to deal with the added extent of cell-cell adhesion. New, more complex dynamics may also appear when the number of cells increases, including changes in cell contact topology (e.g. as studied in [18]); this will be a focus of future work. We show initial snapshots of two cells and three cells persistently rotating within circular micropatterns as well as three cells rotating within a square micropattern in Fig S5.

## 10 Nucleus can influence the cell-cell interface shape

We show in Fig. S6 that the nucleus can influence the cell-cell interface’s shape, even reversing its chirality. However, this reversal can also be accomplished by varying other parameters.

## 11 Parameter setting

Our goal in this paper has been to develop a reasonably generic simplified model of mammalian cell motility that can give some insight into the coordination of rotation. However, we are not attempting to fit specific experiments, and so we will use only rough estimates. Where possible, we have chosen to use parameters consistent with our earlier models [1, 5, 19]. The parameters we use by default throughout this paper are given below, in Table S1. We also briefly discuss the justification of these parameters below.

### 11.1 Cell mechanical parameters

The order of magnitude of the cell tension and bending coefficients was set in [1] by comparison with shear flow experiments on *Dictyostelium* cells [20]. The friction coefficient  $\tau$  was set by [1] by fitting to experimental data on fish keratocytes [21]. Our cell velocities are chosen to be comparable to keratocyte velocities,  $v \sim 0.2\mu\text{m}/\text{s}$  [21]; this sets the characteristic velocity scale, which is  $\alpha\rho^{\text{maximum}}/\tau$ ; with our reaction-diffusion model,  $\rho^{\text{maximum}} \approx 1.4\mu\text{m}^{-2}$ , so this sets the general scale of  $\alpha \approx 0.4pN \mu\text{m}^{-3}$ .  $\beta$  must be chosen so that the highest  $\rho$  in the cell is larger than  $\alpha/\beta$ , and the smallest value is lower than  $\alpha/\beta$ . We also found that choosing  $\beta$  too small prevented the nucleus from being effectively pulled by the contraction of the back of the cell.

### 11.2 Reaction-diffusion parameters

The order of magnitude of the reaction-diffusion parameters was set by comparison to measured Rho GTPase kinetics by [6]; we use the parameters of [19] for the reaction-diffusion mechanism. The dynamics of  $I$  are not chosen to model a specific inhibitor, but merely a plausible diffusing molecule generated by various processes. We therefore choose  $D_I$  to be of the scale of membrane protein and lipid diffusion coefficients,  $D_I = 1\mu\text{m}^2/\text{s}$  [22]. The degradation rate  $k_{-I}$  is at the same timescale as the Rho GTPase kinetics ( $s^{-1}$ ), and has also been chosen to ensure that cell-cell contacts in the CIL mechanism only generate  $I$  near the contact, and not throughout the cell. The noise parameter  $\eta$  is calibrated above.

### 11.3 Polarity mechanism parameters

Our general approach to the polarity mechanism parameters has been to ensure that the mechanisms strongly determine the cell’s polarity, e.g. that in the CIL model, cell-cell contact completely prevents polarity in that direction. We found that choosing  $k_I^{\text{CIL,FF}} = 0.25s^{-1}$  was sufficient to do this. For the neighbor-aligning and velocity-aligning cells,  $k_I^{\text{NA,VA}} = 0.1s^{-1}$  ensures that the direction of high  $\rho$  aligns well with the additional polarity vector  $\hat{\mathbf{p}}$ . In the NA/VA mechanisms, we choose  $T_{\text{orient}}$  to be small relative to the timescale of motion (0.02 s compared with tens of seconds for a cell to crawl its own radius), resulting in a polarity that aligns very quickly with its input (either the cell’s velocity or the velocity of nearby cells).

### 11.4 Cell-cell interaction parameters

The cell-cell repulsion parameter  $g$  sets the energy for a given area of overlap; we choose it as  $1pN/\mu\text{m}$ , or around  $250k_B T$  per square micron; this effectively prevents cell-cell overlap. The adhesion scale  $\sigma$  is chosen to be close to the line tension of the cells, ensuring that cells can easily deform to increase their cell-cell contact.

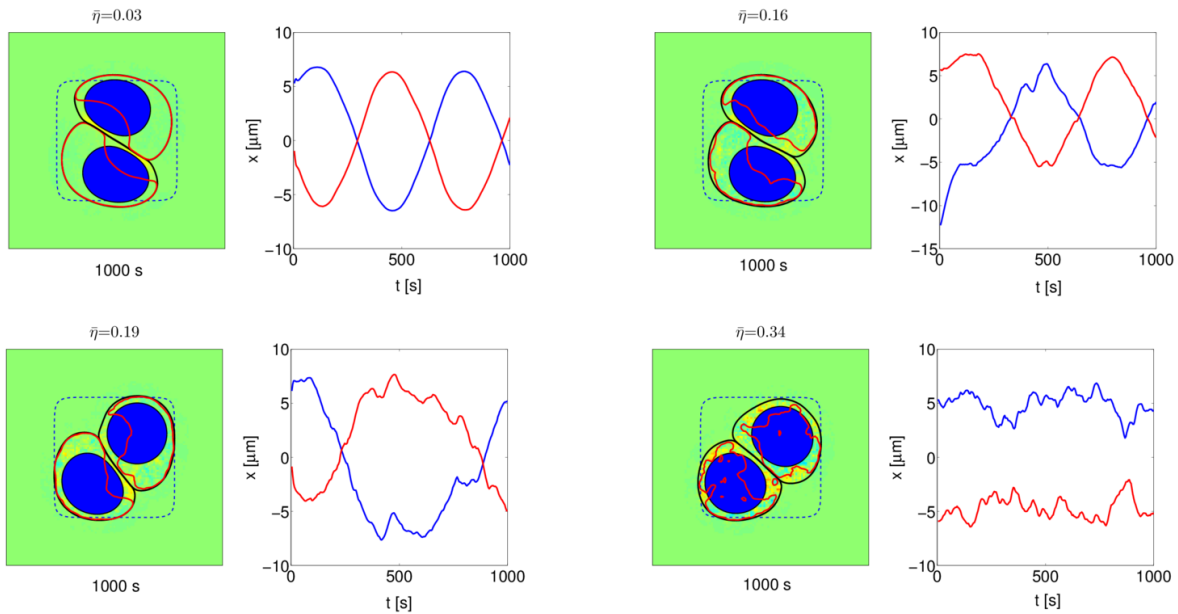


Figure S4: **Decreasing cell persistence disrupts persistent rotational motion.** We show snapshots at 1000 s and traces of each cell's center of mass (projected on the  $x$  axis) over time for four different values of the unitless noise of the inhibitor  $\bar{\eta}^2 = \eta^2/D_I$ . Increasing the noise can cause reversals ( $\bar{\eta} = 0.16$ ) as well as completely suppressing rotation ( $\bar{\eta} = 0.34$ ). These simulations use the FF mechanism and are on a 25-micron adhesive pattern. See also Supplementary Movie S12.

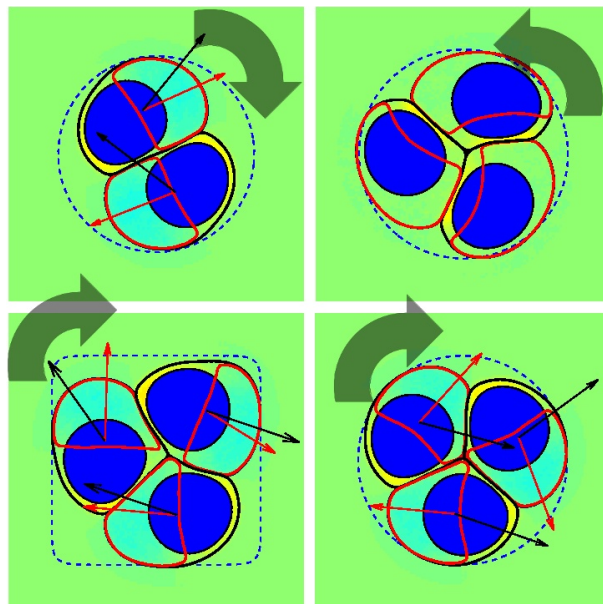


Figure S5: **Our method is simply extended to other patterns and larger numbers of cells.** Here we show snapshots of various extensions to different pattern shapes and larger numbers of cells. These are (upper left) a rotating pair of VA cells on a circular micropattern with diameter  $30\mu m$ , shown at 1000 s, (upper right) three FF cells on a circular micropattern with diameter  $32\mu m$  shown at 1000 s, (lower left) three VA cells on a square micropattern with  $L_{\text{micro}} = 32\mu m$  shown at 720 s, and (lower right) three VA cells on a circular micropattern with diameter  $32\mu m$  shown at 720 s. Parameters are as given in Table S1, except for the three-cell simulations we have used  $\Delta t = 0.0005$  seconds.

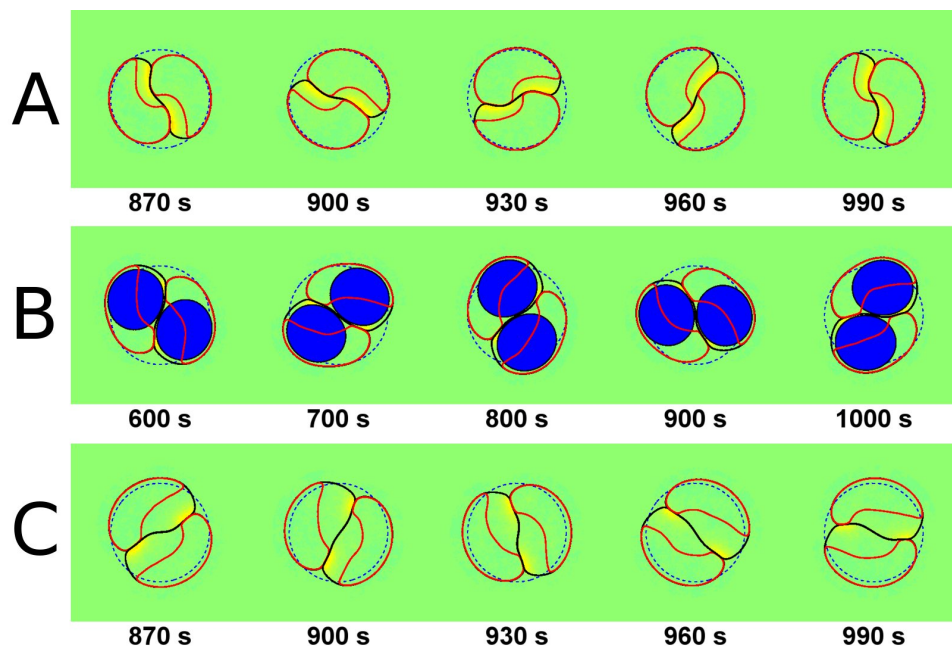


Figure S6: **Nucleus can influence cell-cell interface shape.** We show three time-traces that demonstrate some of the variables contributing to interface shape. We have used a circular micropattern of radius  $12.5 \mu m$ , and simulate cells with the FF mechanism. A: Cell without a nucleus exhibiting PRM with an interface deformed inward in the back. B: Cell with a nucleus exhibiting PRM with an interface bulging outward at the back. The only difference between A and B is that A has no nucleus. Both A and B have slightly different parameters than our defaults;  $\alpha$  is 1.5 times its default value,  $\gamma_{nuc}$  and  $\kappa_{nuc}$  are five times their default value,  $M$  is ten times its default value, and the nuclear radius is  $7.3 \mu m$  ( $\Delta t = 0.001s$ ); these changes are made to highlight the influence of the nucleus. C shows a cell with no nucleus, but with an interface bulging outward at the back. The cell shown in C has  $\alpha$  twice its default value and  $\beta$  half its default value. The interface shapes of B and C are consistent with the experiments of [17], but the shape of A is not.

Table S1: **Table of simulation parameters**

Parameter	Description	Value
$\alpha$	Protrusion coefficient	0.4 pN / $\mu m^3$
$\beta$	Retraction coefficient	0.2 pN / $\mu m$
$\gamma$	Cell tension coefficient	1.8 pN
$\kappa$	Cell bending coefficient	1 pN $\mu m^2$
$g$	Cell-cell body repulsion coefficient	1 pN / $\mu m$
$\sigma$	Cell-cell adhesion coefficient	1.875 pN / $\mu m$
$g_{\text{nuc}}$	Nucleus confinement coefficient	2 pN / $\mu m$
$\gamma_{\text{nuc}}$	Nucleus tension coefficient	2 pN
$\kappa_{\text{nuc}}$	Nucleus bending coefficient	2 pN $\mu m^2$
$R_{\text{nuc}}$	Nucleus radius ( $A_{\text{nuc}} = \pi R_{\text{nuc}}^2$ )	6 $\mu m$
$R_{\text{cell}}$	Initial radius of cell	10 $\mu m$
$M$	Nucleus area constraint multiplier	1 pN / $\mu m^3$
$\tau$	Friction coefficient	2.62 pN s / $\mu m^2$
$\tau_{\text{nuc}}$	Nuclear friction coefficient	1 pN s / $\mu m^2$
$\epsilon$	Phase field width	2 $\mu m$
$k_a$	Unitless base activation rate	0.01
$k_b$	Overall activation rate	10 $s^{-1}$
$k_c$	Deactivation rate	10 $s^{-1}$
$K_a$	Positive feedback threshold for actin promoter (Rho GTPase) concentration	1 $\mu m^{-2}$
$D_\rho$	Actin promoter (Rho GTPase) diffusion coefficient	0.8 $\mu m^2/s$
$N_{\text{tot}}$	Total amount of actin promoter (unitless)	800
$D_I$	Inhibitor diffusion coefficient	1 $\mu m^2/s$
$k_I^{\text{CIL,FF}}$	Rate of $I$ generation from contact inhibition, FF mechanism	0.25 $s^{-1}$
$k_I^{\text{NA,VA}}$	Rate of $I$ generation from neighbor alignment, velocity alignment	0.1 $s^{-1}$
$k_{-I}$	Degradation rate of $I$	0.2 $s^{-1}$
$T_{\text{orient}}$	Time scale for polarity orientation in NA and VA models	0.02 $s$
$\Delta t$	Numerical time step	0.002 $s$
$\bar{\eta}$	Unitless noise strength	0.03
$\zeta$	Alignment noise strength	10 $s^{-1/2}$

These parameters are used throughout the paper; any deviation from them is explicitly noted.

## 11.5 Nucleus parameters

In modeling the nucleus, we have described it as a phase field with a tension, bending modulus, as well as a constraint ensuring that the area of the nucleus is fixed.  $M$  is chosen (much as the similar parameter in [1]) to be large enough that the nuclear area is well-conserved (to around 1%, in a typical simulation). We have chosen the nuclear membrane to have only a slightly higher tension and bending modulus than the cell membrane for computational ease; the largest effect of the nucleus is from its effective incompressibility.  $\tau_{\text{nuc}}$  is set to be slightly smaller than the value  $\tau$ ; we found that significantly larger values of  $\tau_{\text{nuc}}$  could lead to the cell's inability to transport the nucleus.  $g_{\text{nuc}}$  was set to ensure that the nucleus does not cross the membrane; its value is similar to the cell-cell repulsion.

## 12 Variation of parameters

In this section, we show that the trends of the regulation of PRM by cell polarity mechanisms are relatively independent of the particular parameters we choose. We vary model parameters, and report the observed phenotype for each polarity mechanism (CIL,FF,VA,NA). These simulations are performed in the 25-  $\mu m$  square micropatterns, and for each model parameter discussed, we run simulations with that parameter multiplied by factors of 0.5, 0.83, 1.2, and 2. We may adjust the time step for numerical stability; we mark parameter sets with an  $X$  where the required time step was too small to reasonably simulate rotation (below  $5 \times 10^{-4}$  s) We find that robustly, 1) CIL cells do not exhibit persistent rotational

motion, 2) VA and FF cells exhibit PRM unless cells become immotile or fail to polarize, except in the case of zero adhesion (discussed below), and 3) NA cells flock unless they become immotile.

In the table below, the following abbreviations are used: P = persistent rotational motion state, F = flocking state, I = immotile state, X = required time step for numerical stability made simulations prohibitively expensive, NRP = not robustly polarized, OC = cells at opposite sides or corners, U = unrealistic (e.g.  $R_{\text{nuc}} > R_{\text{cell}}$ ), O = other.

Table S2: **Parameter variations: FF polarity mechanism in 25  $\mu\text{m}$  micropattern.** (Typical parameters: P)

Parameter	0.5x	0.83x	1.2x	2x
$\gamma$	P	P	P	NRP,OC (Fig.S7A)
$\kappa$	X	P	P	P
$\alpha$	NRP,OC	P	P	P (Fig.S7B)
$\beta$	P	P	P	P
$\tau$	P	P	P	P
$g$	P	P	P	P
$\sigma$	P	P	P	X
$k_I$	P	P	P	P
$k_{-I}$	P	P	P	P
$D_\rho$	P	P	P	P
$D_I$	P	P	P	P
$x_0$	P	P	P	P
$\gamma_{\text{nuc}}$	P	P	P	P
$\kappa_{\text{nuc}}$	P	P	P	P
$g_{\text{nuc}}$	P	P	P	P
$\tau_{\text{nuc}}$	P	P	P	P
$M$	P	P	P	P
$R_{\text{nuc}}$	P	P	P	U
$N_{\text{tot}}$	I	I	P	NRP,OC
$k_a$	P	P	P	P
$k_b$	I	I	P	P
$K_a$	NRP,OC	P	I	I
$k_c$	P	P	I	I

Table S3: **Parameter variations: CIL polarity mechanism in 25  $\mu\text{m}$  micropattern.** (Typical parameters: OC)

Parameter	0.5x	0.83x	1.2x	2x
$\gamma$	OC	OC	OC	OC
$\kappa$	X	OC	OC	OC
$\alpha$	OC	OC	OC	OC
$\beta$	OC	OC	OC	OC
$\tau$	OC	OC	OC	OC
$g$	OC	OC	OC	OC
$\sigma$	OC	OC	OC	X
$k_I$	OC	OC	OC	OC
$k_{-I}$	OC	OC	OC	OC
$x_0$	OC	OC	OC	OC
$D_\rho$	OC	OC	OC	OC
$D_I$	OC	OC	OC	OC
$\gamma_{\text{nuc}}$	OC	OC	OC	OC
$\kappa_{\text{nuc}}$	OC	OC	OC	OC
$g_{\text{nuc}}$	OC	OC	OC	OC
$\tau_{\text{nuc}}$	OC	OC	OC	OC
$M$	OC	OC	OC	OC
$R_{\text{nuc}}$	OC	OC	OC	U
$N_{\text{tot}}$	I	I	OC	NRP,OC
$k_a$	OC	OC	OC	OC
$k_b$	I	I	OC	OC
$K_a$	NRP,OC	OC	I	I
$k_c$	OC	OC	I	I

Table S4: **Parameter variations: VA polarity mechanism in 25  $\mu\text{m}$  micropattern.** (Typical parameters: P)

Parameter	0.5x	0.83x	1.2x	2x
$\gamma$	P	P	P	P
$\kappa$	X	P	P	P
$\alpha$	P	P	P	P
$\beta$	P	P	P	P
$\tau$	P	P	P	P
$g$	P	P	P	P
$\sigma$	P	P	P	X
$k_I$	P	P	P	P
$k_{-I}$	P	P	P	P
$D_\rho$	P	P	P	P
$D_I$	P	P	P	P
$\gamma_{\text{nuc}}$	P	P	P	P
$\kappa_{\text{nuc}}$	P	P	P	P
$g_{\text{nuc}}$	P	P	P	P
$\tau_{\text{nuc}}$	P	P	P	P
$M$	P	P	P	P
$R_{\text{nuc}}$	P	P	P	U
$N_{\text{tot}}$	I	P	P	P
$k_a$	P	P	P	P
$k_b$	I	P	P	P
$K_a$	P	P	P	I
$k_c$	P	P	P	I

Table S5: **Parameter variations: NA polarity mechanism in 25  $\mu m$  micropattern.** (Typical parameters: F)

Parameter	0.5x	0.83x	1.2x	2x
$\gamma$	F	F	F	F
$\kappa$	X	F	F	F
$\alpha$	F	F	F	F
$\beta$	F	F	F	F
$\tau$	F	F	F	F
$g$	F	F	F	F
$\sigma$	F	F	F	X
$k_I$	F	F	F	F
$k_{-I}$	F	F	F	F
$D_\rho$	F	F	F	F
$D_I$	F	F	F	F
$\gamma_{\text{nuc}}$	F	F	F	F
$\kappa_{\text{nuc}}$	F	F	F	F
$g_{\text{nuc}}$	F	F	F	F
$\tau_{\text{nuc}}$	F	F	F	F
$M$	F	F	F	F
$R_{\text{nuc}}$	F	F	F	U
$N_{\text{tot}}$	I	F	F	F
$k_a$	F	F	F	F
$k_b$	I	F	F	F
$K_a$	F	F	F	I
$k_c$	F	F	F	I

There are several trends worth noting in these tables. The most obvious one is that most parameters are irrelevant to the presence or absence of collective motion, though they may change the morphology of the cells. In particular, none of the nuclear parameters affect the qualitative motility behavior, and neither do the diffusion coefficients  $D_{I,\rho}$ , or the parameters related to the strength of the polarity interaction ( $k_I, k_{-I}, x_0$ ). However, effects that either prevent single cells from polarizing or create large deformations in single-cell shape can inhibit motility. For instance, we note that the ability of the cell to polarize in the FF and CIL models is strongly dependent on the total amount of Rho GTPase,  $N_{\text{tot}}$  - if  $N_{\text{tot}}$  is too small (large),  $\rho$  becomes homogeneous and small (large). This is well-understood as a feature of the reaction-diffusion mechanism [5, 6, 23]. This effect is somewhat weaker in the NA and VA models, because we bias the  $\rho$  dynamics to align with our auxiliary polarity variable  $\hat{\mathbf{p}}$ . Similarly, the ability to polarize depends systematically on the reaction-diffusion parameters for the  $\rho$  model,  $k_a, k_b, K_a, k_c$ . Mechanical parameters may also play a role in prohibiting motility: if  $\alpha$  is too small (weak protrusion) or  $\gamma$  is too large (high tension), cells may not be able to effectively protrude (see, e.g. Fig.S7A). The central point we make here is that the distinction between FF, CIL, VA, and NA is reasonably robust, and deviations from what we present in the main paper are mostly at parameters where cells are not even motile - unrealistic models for the experiments of Huang et al. [17].

Numerical instability is an issue in two specific cases: large  $\sigma$  and small  $\kappa$ . In our phase-field equations for  $\phi$ , we have two terms that are fourth order in gradients: one proportional to  $\kappa$ , derived from membrane bending, which is handled implicitly, and one from cell-cell adhesion, proportional to  $\sigma$ , handled explicitly (see Section 13). When the explicitly-handled term dominates, we have numerical difficulties; these may be resolved by increasing  $\kappa$ . In the cases of large  $\sigma$  and small  $\kappa$ , we have not been able to choose a high enough time step to robustly identify behavior. In addition, in these cases, we see lattice artifacts where cell-cell interfaces prefer to align along particular orientations in space.

We point out a few interesting cases in Fig.S7 which are also noted in the table above. In case A, the tension  $\gamma$  is increased by a factor of two in the FF model, leading to effectively circular cells. In this case, no PRM is created, and only one cell at a time is polarized; this oscillates sporadically. In B, the protrusion strength  $\alpha$  is increased by a factor of two in the FF model. This is a case where the morphology of the cell-cell pair appears different - with a larger spread area. This may more closely correspond to the experiments of Huang et al. [17]. We also show in Fig.S7C a case without adhesion ( $\sigma = 0$ ); NA, CIL, and VA maintain their phenotypes (though CIL cells do not remain in contact), but the FF mechanism requires persistent cell-cell contact to drive PRM, and PRM is absent if there is no adhesion.

From these parameter variation studies, we argue that the distinctions between CIL, FF, NA, and VA polarity mechanisms are robust, and that the parameters presented in the main paper are reasonably representative. This suggests that the fundamental nature of the polarity mechanism qualitatively regulates the existence of PRM.

### 13 Numerical details

We describe briefly some of the important details in our numerical solution of these equations. We will mostly discuss these in the single-cell case; the multi-cell case is a simple generalization.

We solve the phase field equation in a semi-implicit spectral fashion (e.g. [24]), handling the high-order derivatives from the single-cell bending and tension terms implicitly, but all other terms explicitly. For a single cell, the phase field equation is (expanding the functional derivative),

$$\partial_t \phi(\mathbf{r}, t) = \frac{1}{\tau} [\alpha \chi(\mathbf{r}) \rho(\mathbf{r}) - \beta] |\nabla \phi| + \frac{\gamma}{\tau} \left[ \nabla^2 \phi - \frac{G'(\phi)}{\epsilon^2} \right] - \frac{\kappa}{\tau} \left[ \nabla^2 - \frac{G''(\phi)}{\epsilon^2} \right] \left[ \nabla^2 \phi - \frac{G'(\phi)}{\epsilon^2} \right]. \quad (\text{S24})$$

We define the explicitly-handled part of this equation as

$$F_{\text{exp}}(t) = \frac{1}{\tau} [\alpha \chi(\mathbf{r}) \rho(\mathbf{r}) - \beta] |\nabla \phi| - \frac{\gamma}{\tau} \frac{G'(\phi)}{\epsilon^2} + \frac{\kappa}{\tau} \nabla^2 \left[ \frac{G'(\phi)}{\epsilon^2} \right] + \frac{\kappa}{\tau} \frac{G''(\phi)}{\epsilon^2} \left[ \nabla^2 \phi - \frac{G'(\phi)}{\epsilon^2} \right]. \quad (\text{S25})$$

We then can write the semi-implicit form

$$\phi(\mathbf{r}, t + \Delta t) - \frac{\Delta t \gamma}{\tau} \nabla^2 \phi(\mathbf{r}, t + \Delta t) + \frac{\Delta t \kappa}{\tau} \nabla^4 \phi(\mathbf{r}, t + \Delta t) = \phi(\mathbf{r}, t) + \Delta t F_{\text{exp}}(t) \quad (\text{S26})$$

which can be easily solved by Fourier transforming:

$$\phi(\mathbf{q}, t + \Delta t) = \frac{\phi(\mathbf{q}, t) + \Delta t \{F_{\text{exp}}(t)\}_{\mathbf{q}}}{1 + (\Delta t \gamma / \tau) q^2 + (\Delta t \kappa / \tau) q^4} \quad (\text{S27})$$

where  $\{\dots\}_{\mathbf{q}}$  indicates a Fourier transform. We move between real and Fourier space using the Fast Fourier Transform. In the multi-cell case, we handle all adhesion terms explicitly.

We solve the reaction-diffusion equations explicitly, using the same time-stepping algorithm presented in [5], but with one modification for the presence of stochastic noise. To solve the stochastic differential equation for  $I(\mathbf{r})$ , we use a simple Euler-Maruyama method [25] combined with the stepping used in [5]:

$$I(t + \Delta t) = \frac{2\phi(t) - \phi(t + \Delta t)}{\phi(t)} I(t) + \Delta t \frac{\nabla \cdot [\phi(t) D_I \nabla I(t)]}{\phi(t)} + \Delta t f_{I, \text{deterministic}} [I(t), \{\phi(t)\}, \dots] + \Xi(\mathbf{r}, \Delta t). \quad (\text{S28})$$

We only divide by  $\phi(t)$  in the region where  $\phi(t) \geq \lambda$ , where  $\lambda = 10^{-4}$ . Outside of this region, we set  $I(t+\Delta t) = I(t)\phi(t)$ . Here,  $\Xi(\mathbf{r}, \Delta t) = \int_t^{t+\Delta t} dt' \xi(\mathbf{r}, t')$  is a Gaussian random variable with zero mean and variance  $\langle \Xi(\mathbf{r}, \Delta t) \Xi(\mathbf{r}', \Delta t) \rangle = \eta^2 \Delta t \delta(\mathbf{r} - \mathbf{r}')$ ; here  $\delta(\mathbf{r})$  is the Dirac delta function. We want to represent this delta function, which is continuous, on our grid. To do this, we need to ensure that our representation maintains the normalization of the Dirac delta function  $\int d^2r \delta(\mathbf{r}) = 1$ . On a square lattice with spacing  $\Delta x$ , this would be  $\int d^2r \delta(r) \rightarrow \sum_{\text{sites } \mathbf{r}} \Delta x^2 \tilde{\delta}_{\mathbf{r}} = 1$ . This suggests that we choose  $\tilde{\delta}_{\mathbf{r}}$  as the Kronecker delta divided by  $\Delta x^2$ , i.e.  $\tilde{\delta}_{\mathbf{r}} = \Delta x^{-2} \delta_{\mathbf{r},0}$ . We therefore choose our noise  $\Xi(\mathbf{r}, \Delta t)$  to be uncorrelated between lattice sites, with each grid point having a variance of  $\eta^2 \Delta t \Delta x^{-2}$ . The  $\rho$  equation is solved with the same stepping described in Eq.S28, though without a stochastic term.

We also do not solve the phase field equation and reaction-diffusion equations in the entire domain; we only solve these equations in a box near each cell. This box is recentered if the cell is close to the boundary of this box: if  $\phi \geq 0.5$  within ten pixels of the boundary, the box is shifted 20 pixels. (The new pixels at the edge of the box are created either as zero (for  $\rho, I, \nu$ ) or by a periodic shift ( $\phi$ ); we expect these details far away from the cell to be irrelevant.) The small box surrounding each cell is  $50 \mu\text{m} \times 50 \mu\text{m}$  ( $128 \times 128$  points). We treat the small box as having periodic boundary conditions, which is appropriate as we keep the cell from too closely approaching the edge. The whole system is  $100 \mu\text{m} \times 100 \mu\text{m}$  ( $256 \times 256$ ). To construct terms such as  $\sum \phi_j$ , which involve sums over many individual fields, we assume that each  $\phi_i = 0$  outside of the box it is defined in. This technique will allow us to increase the size of the system and the number of cells studied in the future.

## References

- [1] Danying Shao, Wouter-Jan Rappel, and Herbert Levine. Computational model for cell morphodynamics. Physical Review Letters, 105(10):108104, 2010.
- [2] Anne-Florence Bitbol and Jean-Baptiste Fournier. Forces exerted by a correlated fluid on embedded inclusions. Physical Review E, 83(6):061107, 2011.
- [3] Pierre C Hohenberg and Bertrand I Halperin. Theory of dynamic critical phenomena. Reviews of Modern Physics, 49(3):435, 1977.
- [4] Charles W Wolgemuth, Jelena Stajic, and Alex Mogilner. Redundant mechanisms for stable cell locomotion revealed by minimal models. Biophysical Journal, 101(3):545–553, 2011.
- [5] Brian A Camley, Yanxiang Zhao, Bo Li, Herbert Levine, and Wouter-Jan Rappel. Periodic migration in a physical model of cells on micropatterns. Physical Review Letters, 111(15):158102, 2013.
- [6] Y. Mori, A. Jilkine, and L. Edelstein-Keshet. Wave-pinning and cell polarity from a bistable reaction-diffusion system. Biophysical Journal, 94(9):3684, 2008.
- [7] Gillian L Ryan, Naoki Watanabe, and Dimitrios Vavylonis. A review of models of fluctuating protrusion and retraction patterns at the leading edge of motile cells. Cytoskeleton, 69(4):195, 2012.
- [8] Jun Allard and Alex Mogilner. Traveling waves in actin dynamics and cell motility. Current Opinion in Cell Biology, 25, 2013.
- [9] Changji Shi, Chuan-Hsiang Huang, Peter N Devreotes, and Pablo A Iglesias. Interaction of motility, directional sensing, and polarity modules recreates the behaviors of chemotaxing cells. PLoS Computational Biology, 9(7):e1003122, 2013.
- [10] Alain Karma and Wouter-Jan Rappel. Quantitative phase-field modeling of dendritic growth in two and three dimensions. Physical Review E, 57(4):4323, 1998.
- [11] Makiko Nonomura. Study on multicellular systems using a phase field model. PloS ONE, 7(4):e33501, 2012.
- [12] Balint Szabo, GJ Szöllösi, B Gönci, Zs Jurányi, David Selmecki, and Tamás Vicsek. Phase transition in the collective migration of tissue cells: experiment and model. Physical Review E, 74(6):061908, 2006.
- [13] Markus Basan, Jens Elgeti, Edouard Hannezo, Wouter-Jan Rappel, and Herbert Levine. Alignment of cellular motility forces with tissue flow as a mechanism for efficient wound healing. Proceedings of the National Academy of Sciences, 110(7):2452, 2013.
- [14] Brian A Camley and Wouter-Jan Rappel. Velocity alignment leads to high persistence in confined cells. Physical Review E, 89:062705, 2014.
- [15] Silke Henkes, Yaouen Fily, and M Cristina Marchetti. Active jamming: self-propelled soft particles at high density. Physical Review E, 84(4):040301, 2011.

- [16] Tamás Vicsek, András Czirók, Eshel Ben-Jacob, Inon Cohen, and Ofer Shochet. Novel type of phase transition in a system of self-driven particles. Physical Review Letters, 75(6):1226, 1995.
- [17] S Huang, CP Brangwynne, KK Parker, and DE Ingber. Symmetry-breaking in mammalian cell cohort migration during tissue pattern formation: role of random-walk persistence. Cell Motility and the Cytoskeleton, 61(4):201, 2005.
- [18] Dapeng Bi, Jorge H Lopez, JM Schwarz, and M Lisa Manning. Energy barriers and cell migration in densely packed tissues. Soft Matter, 10(12):1885, 2014.
- [19] D. Shao, H. Levine, and W.-J. Rappel. Coupling actin flow, adhesion, and morphology in a computational cell motility model. Proceedings of the National Academy of Sciences, 109(18):6851, 2012.
- [20] Rudolf Simson, Eva Wallraff, Jan Faix, Jens Niewöhner, Günther Gerisch, and Erich Sackmann. Membrane bending modulus and adhesion energy of wild-type and mutant cells of dictyostelium lacking talin or cortexillins. Biophysical Journal, 74(1):514, 1998.
- [21] Kinneret Keren, Zachary Pincus, Greg M Allen, Erin L Barnhart, Gerard Marriott, Alex Mogilner, and Julie A Theriot. Mechanism of shape determination in motile cells. Nature, 453(7194):475, 2008.
- [22] Marten Postma, Leonard Bosgraaf, Harriët M Loovers, and Peter JM Van Haastert. Chemotaxis: signalling modules join hands at front and tail. EMBO Reports, 5(1):35, 2004.
- [23] Y. Mori, A. Jilkine, and L. Edelstein-Keshet. Asymptotic and bifurcation analysis of wave-pinning in a reaction-diffusion model for cell polarization. SIAM Journal on Applied Mathematics, 71(4):1401, 2011.
- [24] LQ Chen and Jie Shen. Applications of semi-implicit fourier-spectral method to phase field equations. Computer Physics Communications, 108(2):147, 1998.
- [25] Peter E Kloeden and Eckhard Platen. Numerical solution of stochastic differential equations, volume 23. Springer, 1992.

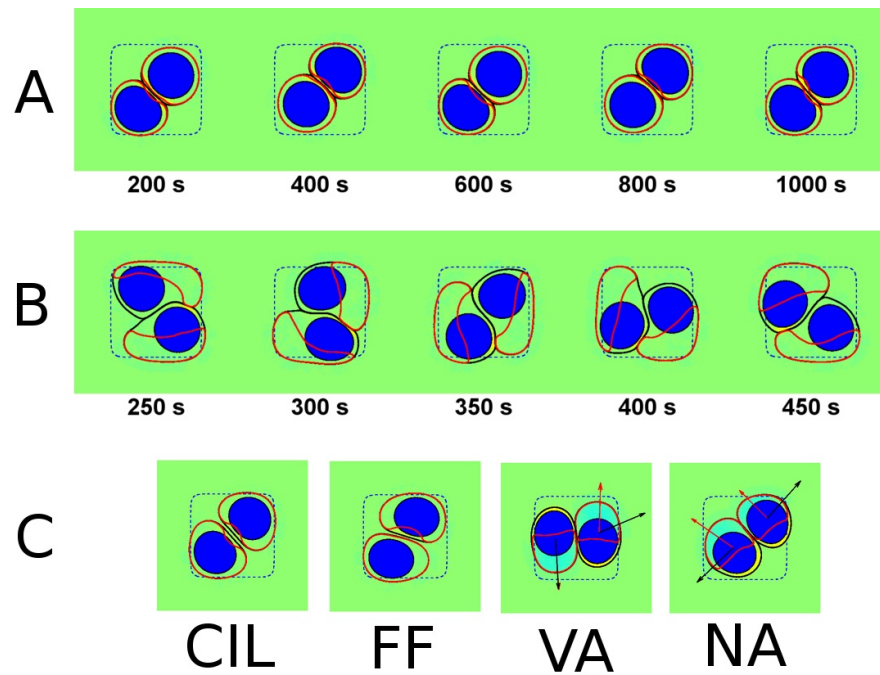
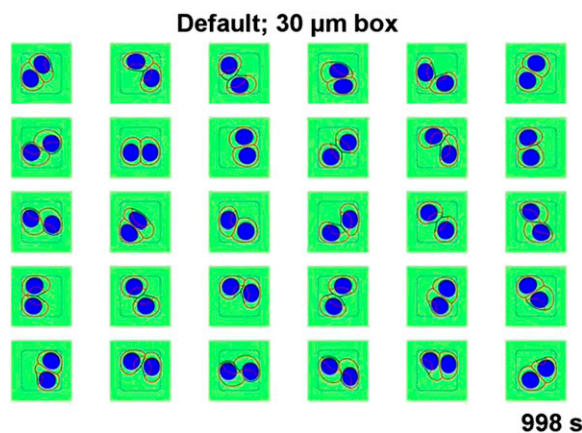


Figure S7: **Interesting phenotypes arising from parameter variations.** These simulations are (A) FF with  $\gamma$  twice its default value, (B) FF with  $\alpha$  twice its default value. In (C) we set  $\sigma = 0$ , i.e. completely turn off adhesion and show snapshots at 1000 seconds for CIL, FF, VA, and NA. Parameters not specified are as in Table S1, with  $L_{\text{micro}} = 25\mu\text{m}$ .

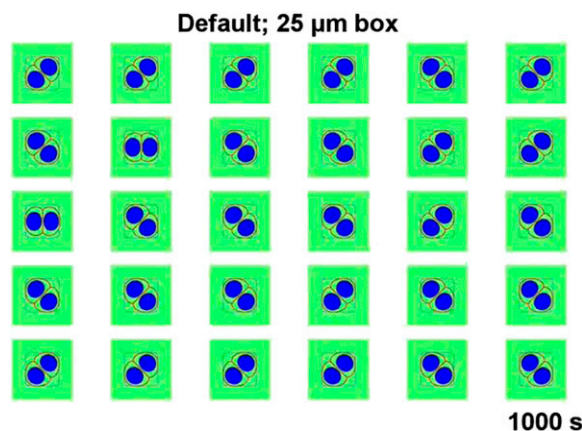
# Supporting Information

Camley et al. 10.1073/pnas.1414498111



**Movie S1.** Simulation of cells with default polarity, 30 micron box. We show thirty simulations of a pair of cells confined in micropatterns of size  $L_{\text{micro}} = 30 \mu\text{m}$  with the default polarity mechanism and a nucleus. These pairs have identical parameters, but different initial conditions as described in the text. Persistent rotation appears, but is not robust.

[Movie S1](#)



**Movie S2.** Simulation of cells with default polarity, 25 micron box. We show thirty simulations of a pair of cells confined in micropatterns of size  $L_{\text{micro}} = 25 \mu\text{m}$  with the default polarity mechanism and a nucleus. These pairs have identical parameters, but different initial conditions as described in the text. No persistent rotation appears, as the cells are unable to polarize.

[Movie S2](#)

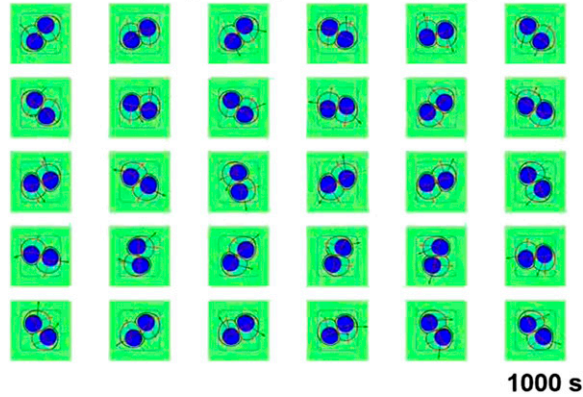






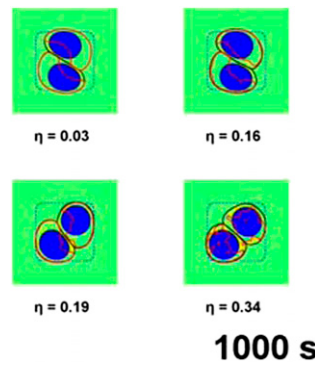


### Velocity alignment; 30 $\mu\text{m}$ box; larger $\zeta$



**Movie S11.** We show thirty simulations of a pair of cells confined in micropatterns of size 30  $\mu\text{m}$ . These cells use the velocity alignment mechanism (VA). These pairs have identical parameters, but different initial conditions as described in the text. In addition  $\zeta$  is 1.5 times its default value. Cells robustly show persistent rotational motion.

[Movie S11](#)



**Movie S12.** Varying cell persistence can change rotational dynamics. We show simulations of pairs of cells with four different noise levels  $\bar{\eta} = 0.03, 0.16, 0.19,$  and  $0.34$ , corresponding to different persistence times. The micropattern size is  $L_{\text{micro}} = 25 \mu\text{m}$  and the cells shown here use the front-front inhibition mechanism (FF).

[Movie S12](#)

## Other Supporting Information Files

[SI Appendix \(PDF\)](#)